LRP 550/96 July 1996

Contributed Papers
presented at the
23rd EPS CONFERENCE ON CONTROLLED
FUSION AND PLASMA PHYSICS

Kiev, Ukraine
24th - 28th June, 1996

LIST OF CONTENTS

EXTERNAL KINK MODE STABILITY OF TOKAMAKS WITH FINITE EDGE CURRENT DENSITY IN PLASMA OUTSIDE SEPARATRIX

L.Degtyarev, A.Martynov, **S.Medvedev**
Keldysh Institute of Applied Mathematics, Russian Academy of Sciences, Moscow

F.Troyon, L.Villard
Centre de Recherches en Physique des Plasmas, Association Euratom – Confédération Suisse, Ecole Polytechnique Fédérale de Lausanne

Abstract

Large pressure gradients and current density at the plasma edge and accompanying edge-localized MHD instabilities are typical for H-mode discharges. Low-n external kink modes are a possible cause of the instabilities. The paper mostly deals with external kink modes driven by a finite current density at the plasma boundary (so called peeling modes). It was shown earlier that for a single axis plasma embedded into vacuum the peeling modes are stabilized when separatrix is approaching the plasma boundary [1]. For doublet configurations a finite current density at the internal separatrix does not necessarily lead to external kink instability when the current density vanishes at the boundary.

However, a finite current density at the plasma boundary outside the separatrix can drive outer peeling modes. The stability properties and structure of these modes depend on the plasma equilibrium outside the separatrix. The influence of plasma shear and pressure gradient at the boundary on the stability of the outer peeling modes in doublets is studied.

The stability of kink modes in divertor configurations with plasma outside the separatrix is very sensitive to the boundary conditions set at open field lines. The choice of the boundary conditions and kink mode stability calculations for the divertor configurations are discussed.

1 Equilibria Doublet equilibria with the same boundary as in [2] (aspect ratio $A = 3.8$, elongation $\kappa = 3.2$) was used in the computations.

The plasma profiles, with pressure gradient having a maximum at the separatrix and finite separatrix current density, were prescribed by

$$I^* = \begin{cases} 1-(1-I_s)\bar{\psi}_{in}, \\ I_s(1-\bar{\psi}_{out}), \end{cases}, \quad p' = \begin{cases} p_0\bar{\psi}_{in}, & \text{inside separatrix} \\ p_0(1-\bar{\psi}_{out}), & \text{outside separatrix} \end{cases}, \tag{1}$$

where I^* is the surface averaged toroidal current density, $0 < \bar{\psi}_{in,out} < 1$ are the normalized poloidal fluxes inside and outside the separatrix, respectively, I_s controls the value of the current density at the separatrix, p_0 controls the maximal value of the pressure gradient at the separatrix.

A series of three doublet equilibria with $I_s = 0.1$ and different values of p_0 is used for stability calculations. The aspect ratio and the elongation of the single axis plasma inside the separatrix are $A = 4.6, \kappa = 1.7$ for all the equilibria. The normalized current and beta values are respectively $I_N = 1.31, 1.28, 1.24, \beta = 0\%, 1.68\%, 3.1\%$ for a safety factor at the magnetic axis $q_0 = 1.05$. The profiles inside and outside the separatrix are given in Fig.1.

2 Peeling mode stability Equilibria with a current density pedestal at the plasma boundary are characteristic for the H-mode regimes in divertor tokamak plasmas. A whole range of MHD phenomena accompany the discharges, in particular the roll-over effect in JET, is associated with low-n external kink peeling modes [3, 4].

On the other hand the kink mode stability computations of single axis plasma with a separatrix at the boundary showed stability of the peeling modes [1]. However, if

the plasma outside the separatrix is still sufficiently conducting and a current density pedestal exists at the plasma edge outside the separatrix then a different sort of ideal MHD instabilities — outer peeling modes can be driven unstable.

Peeling modes are unstable when a current density pedestal exists at the plasma boundary and a rational magnetic surface is located in vacuum close to the boundary (edge safety factor $q_s < m/n$). The following procedure is used to study the outer peeling mode stability dependence on shear and β. The external plasma layers are "scraped" to produce the edge current density pedestal from the profiles (1). Then the value of q_0 is adjusted to get the value of $q_s < m/n$ and the unstable range in the q_s values is estimated. The conducting wall is chosen with the wall/plasma minor radius ratio more than 2 and the effect of wall stabilization was weak enough.

The Fig.2 shows the $n = 1$ mode unstable ranges of $q_s < 3$ for the single axis plasmas inside the separatrix embedded in vacuum with the boundaries defined by different values of $\psi_s \leq 1$ indicating the normalized poloidal flux left in plasma. The value of $\psi_s = 1$ corresponds to the separatrix at the boundary. Let us note that the current density pedestal for the single axis plasma is higher than $I_s = 0.1$ for $\psi_s < 1$. The unstable range in the q_s values shrinks as ψ_s approaches 1 giving the stability for $\psi_s = 1$. No pressure stabilization was observed in contrast to [4]. A possible explanation to that is different plasma geometry and profiles. The averaged curvature stabilization which can be derived from the localized peeling mode stability criterion [5] is absent for the considered equilibria.

The Fig.3 shows the $n = 1$ mode unstable range of $q_s < 6$ for the doublet plasmas. The values of ψ_s indicate the normalized flux in the plasma outside the separatrix in this case. The q-profile is nonmonotonic in the plasma outside the separatrix and there exists a region of negative shear (Fig.1). The peeling mode criterion indicates stability of localized external modes in a region of negative shear. In general the global mode stability should not follow the localized mode criterion. However, for $\beta = 0$ the marginally stable values of ψ_s for localized and global modes in the region of negative shear are quite close to each other (see Fig.3a). The stability window at $\psi_s \to 1$ corresponds to the decreasing current pedestal which vanishes for $\psi_s = 1$.

The finite beta effect on the outer peeling mode stability is shown in Fig.3b. The stability window grows and the unstable q_s range is smaller. At the same time the stability window in ψ_s values given by the localized mode stability criterion is getting narrower with higher beta.

The mode structure of the unstable displacements is that of typical peeling mode for $\psi_s \simeq 1$ and is less localized for the values of ψ_s near $q'(\psi) = 0$ (Fig.4).

3 Stability of divertor configurations

The divertor equilibria with plasma outside the separatrix were "cut" from the doublet equilibria computed with the CAXE code in the same way as in [2]. The stability code KINX-W has been modified to include a Green's function technique vacuum treatment for the modes $n \neq 0$.

A characteristic feature of the divertor configuration is the presence of open magnetic field lines penetrating the end plates. Boundary conditions there have a strong effect on the plasma stability properties. Vanishing displacement condition at the end plates was used in [2] for axisymmetric $n = 0$ mode stability calculations. However, in the case of external kink modes these conditions lead to an unrealistic strong stabilizing effect. Our computations showed the stability of all external kink modes except the analog of $m = 1$, $n = 1$ external mode for very high values of normalized current corresponding to the Kruskal–Shafranov stability limit $q < 1$.

The ideal MHD energy principle is valid when the vanishing displacement condition at the end plates is assumed. The perturbed plasma normal magnetic field $\delta\mathbf{B} = \nabla \times (\xi \times \mathbf{B})$ also vanishes at the end plates in this case, where ξ is the plasma displacement, $\mathbf{B}$ is the equilibrium magnetic field. This gives the boundary condition for the perturbed magnetic field in vacuum $\delta\mathbf{B}_v \cdot \mathbf{n} = 0$.

The formulation becomes more complicated with finite displacement at the end plates.

In this case one extra term enters the weak formulation of the stability problem $1/2 \int_S \tilde{\xi} \cdot \delta \mathrm{B}_v (\mathbf{n} \cdot \mathrm{B}) dS$ making the problem non selfadjoint. When both perturbed normal vacuum magnetic field and tangential plasma displacement at the end plates vanish the extra term drops out. However, the analysis shows that zero tangential displacement at the end plates is not sufficient to make the normal perturbed plasma magnetic field vanish for $n \neq 0$. So the formulation with free normal displacement at the end plates is selfadjoint but not fully self consistent.

No divertor analogs of the outer peeling mode have been discovered up to now. Further investigation is needed to get a conclusive answer on the outer mode stability in divertor configurations.

4 Conclusions The outer peeling modes were studied in the doublet tokamak plasma with H-mode like profiles. The computations show that the modes are stable when the mantle plasma outside the separatrix is thin enough despite the current density pedestal. As the mantle is getting thicker the outer peeling mode with distributed structure appears. This mode can be stabilized at finite β.

The choice of the boundary conditions plays a major role in the stability of divertor plasma configurations. Realistic stability problem formulation for the equilibria with open magnetic field lines should be worked out.

References

[1] Boucher D. *et al.* ITER plasma modeling and MHD stability limits, 15th Int. Conf. on Plasma Phys. and Controlled Nuclear Fusion Research, Sevilla, Spain, September–October (1994), paper IAEA-CN-60/E-P-2

[2] Degtyarev L.M., Martynov A., Medvedev S., Troyon F., Villard L. Influence of plasma near separatrix on ideal MHD stability in tokamaks 22th EPS Conf. on Controlled Fusion and Plasma Phys., Bournemouth, Proc. Contrib. Papers, Vol.19C(1995), Part I, p.217

[3] Smeulders P., Alper B., Bak P. *et al.* Influence of MHD instabilities on JET high performance, 22th EPS Conf. on Controlled Fusion and Plasma Phys., Bournemouth, Proc. Contrib. Papers, Vol.19C(1995), Part IV, p.61

[4] Huysmans G.T.A., Chalis C.D., Erba M. *et al.* Influence of edge currents and pressure gradients on the MHD stability of low-n external kink modes, 22th EPS Conf. on Controlled Fusion and Plasma Phys., Bournemouth, Proc. Contrib. Papers, Vol.19C(1995), Part I, p.201

[5] Wesson J.A. Hydromagnetic stability of tokamaks, Nucl. Fusion, Vol.18(1978), p.87

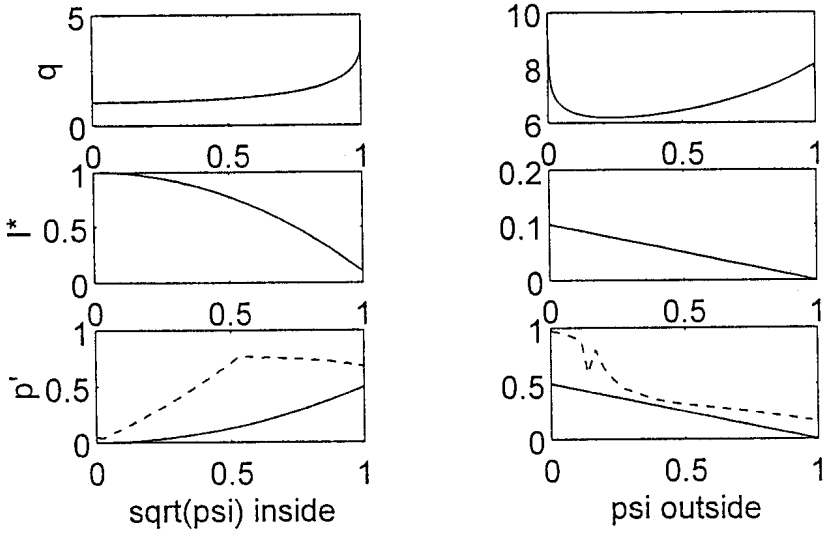

Fig.1. Plasma parameter profiles for the doublet equilibrium with $\beta = 1.68\%$. Pressure gradient profile locally optimized against ballooning mode stability is shown by a dashed line.

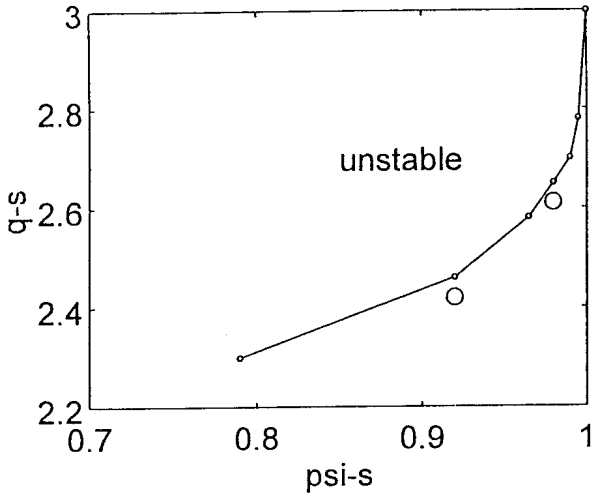

Fig.2. Peeling mode $n = 1$ instability region $q_s \leq 3$ for single axis plasma versus the value of normalized poloidal flux ψ_s left in the plasma. The points correspond to $\beta = 0$, the circles – to $\beta = 1.68\%$.

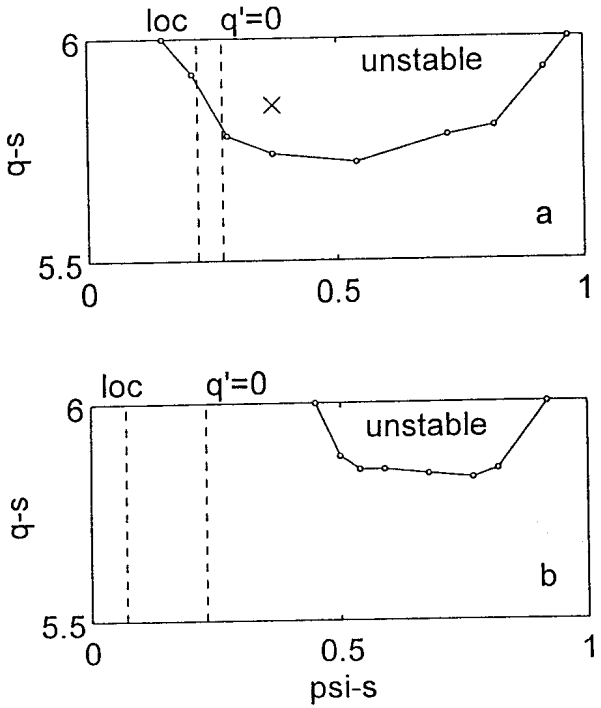

Fig.3. Outer peeling mode $n = 1$ instability region $q_s \leq 6$ for doublet plasmas versus the value of normalized poloidal flux ψ_s left in the mantle plasma. The locations of the safety factor minimum and marginally stable value of ψ_s for localized peeling mode criterion are marked.
a) $\beta = 0\%$ b) $\beta = 1.68\%$

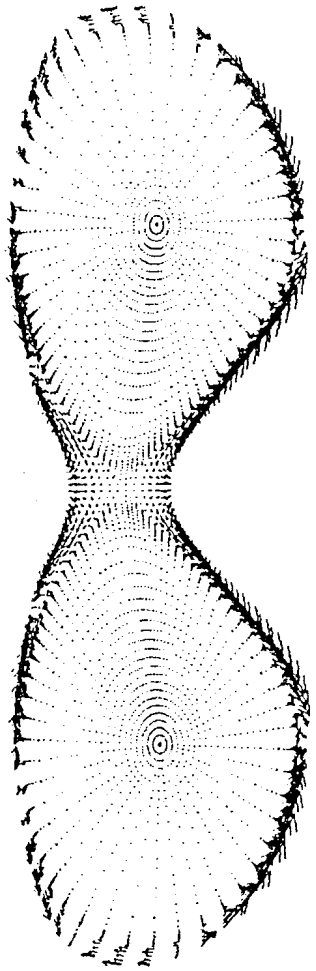

Fig.4. Outer peeling mode arrow plot for the doublet configuration marked by the cross in Fig.3,a. $q_0 = 1.05, q_s = 5.66; q_{min} = 5.57$ in the mantle region. Growth rate $\gamma/\gamma_A = 1.38 \cdot 10^{-2}$.

How the Shape Influences the TCV Plasma Properties

J.-M. Moret, M. Anton, R. Behn, F. Bühlmann, M.J. Dutch, B.P. Duval, A. Fasoli, S. Franke, F. Hofmann, B. Joye, J.B. Lister, Y. Martin, C. Nieswand, Z.A. Pietrzyk, R.A. Pitts, A. Pochelon, F.N. Skiff, W. van Toledo, G. Tonetti, M.Q. Tran, H. Weisen

Centre de Recherches en Physique des Plasmas
Association EURATOM - Confédération Suisse
École Polytechnique Fédérale de Lausanne, CH-1015 Lausanne, Switzerland

TCV has the unique capability of creating a wide variety of plasma shapes [1], controlled by 16 independent coils. This opens a new domain in Tokamak operation which has been explored to investigate the influence of the shape on plasma properties. In limited ohmic L-mode stationary discharges (R = 0.88 m, a = 0.25 m, B_T = 1.4 T), the following parameters have been systematically scanned:

elongation	$\kappa = 1.1 \rightarrow 1.9$	edge safety factor	$q_a = 2 \rightarrow 6$
triangularity	$\delta = -0.45 \rightarrow 0.75$	line average density	$n_e = 2.5 \rightarrow 8.5 \times 10^{19}$ m^{-3}

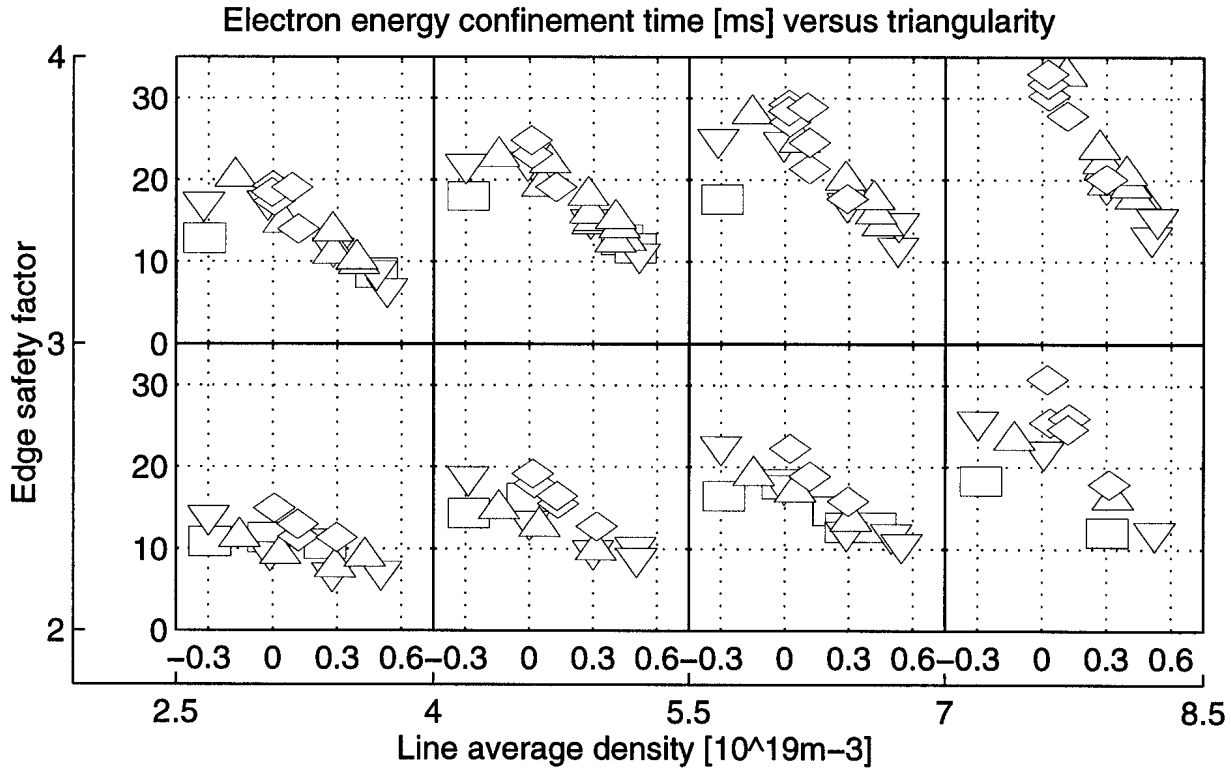

Fig. 1. Dependence of the electron energy confinement time on the shape for 4 classes of density and 2 classes of safety factor. The horizontal axis in each plot is the triangularity. Symbols represent the elongation: □ $\kappa = 1 \rightarrow 1.25$, ▽ $\kappa = 1.25 \rightarrow 1.5$, △ $\kappa = 1.5 \rightarrow 1.75$, ◇ $\kappa = 1.75 \rightarrow 2$.

The confinement properties of these plasmas are quantified by the electron energy confinement time, $\tau_{Ee} = W_e/P_{oh}$, where P_{oh} is the ohmic input power. The total electron energy, W_e, is obtained by volume integration of Thomson scattering measurements at 10 spatial positions.

The ratio P_{rad}/P_{oh} was observed to be remarkably constant in all conditions [2] so a correction for the total radiated power P_{rad} does not modify the observed variations in τ_{Ee}. For a given plasma shape, τ_{Ee} exhibits the usual increase with q_a and the usual linear dependence on the density (fig. 1); the density saturation occurs at values slightly higher than the highest one used in this work. In all conditions a strong dependence of τ_{Ee} on the plasma shape was found: a slight improvement with elongation and a marked degradation with positive triangularity, both at fixed value of q_a (fig. 1). The degradation factor over the scanned triangularity range is typically 2 and reaches 3 at the highest density. The improved confinement at negative triangularity leads to a reduction in the ohmic power which is necessary to drive the plasma current. This is also reflected in reduced sawtooth ramp rates, which are proportional to the central ohmic power deposition in all conditions. The electron energy confinement keeps increasing when going to negative triangularity so that the influence of triangular shape is not symmetric. Some data points however indicate a reduced confinement correlated with MHD activity seen both on magnetic probes and soft X-ray tomography.

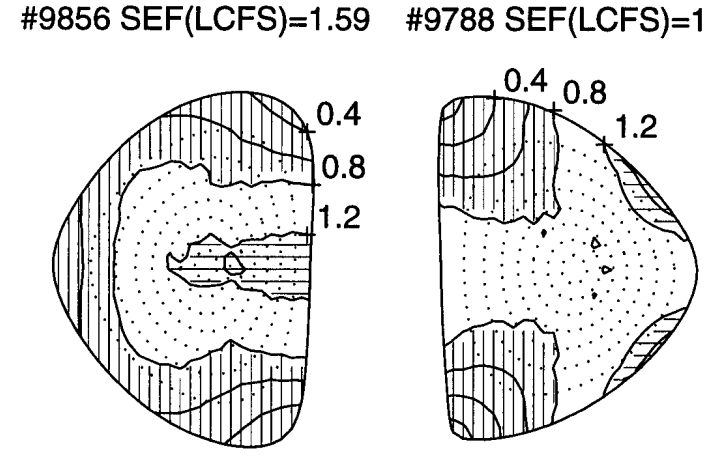

Fig. 2. Distribution of the gradient geometrical factor for a negative (left) and positive (right) triangularity. Vertical and horizontal hatching shows the reduced and increased gradient regions respectively.

Geometrical effects. A direct consequence of the shaping is a modification of the flux surface separation and incidently of the gradients. This will influence the conducted energy fluxes $q = -n\chi \nabla T$. The density n, the thermal diffusivity χ and the temperature T of both the ions and the electrons are assumed constant on a poloidal flux (ψ) surface. The usual choice of the normalised flux coordinate is not satisfactory since it depends on the current distribution. To circumvent this effect the profiles were mapped on to the equatorial plane. The energy flux becomes $-n\chi$ (dT/dr*) (dr*/dψ) $\nabla\psi$ where r* is the outer horizontal distance from the magnetic axis normalised such that it equals the minor radius (half the horizontal plasma width) on the last closed flux surface (LCFS). This mapping was necessary to handle flux surface compression in the outer equatorial plane due to negative triangularity and Shafranov shift. The spatial distribution of the geometrical factor (dr*/dψ) $\nabla\psi$ is plotted in figure 2 for two shapes: a value smaller than unity implies smaller gradients compared to a cylindrical plasma of same horizontal width. This plot allows to identify the regions where energy fluxes are increased or decreased. In particular, the compression of flux surfaces toward the outer tip of a positive triangularity shape creates an extended region with increased gradients. At negative triangularity, this region shrinks due to increasing separation of the flux surfaces away from the equatorial plane, so that a large part of the plasma can benefit from shaping geometrical effects. Only the surface integral of the energy flux enters the 1-D

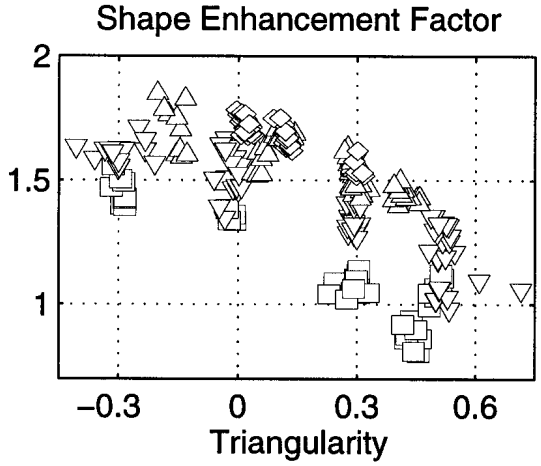

Fig. 3. Shape enhancement factor on the LCFS. See fig. 1 for symbols.

radial power balance and it is therefore convenient to define a shape enhancement factor (SEF) $s = d\psi/dr^* \langle\nabla\psi\rangle^{-1}$, where the average is taken on a flux surface. The value of the SEF on the LCFS is shown in figure 3 for all the shapes studied, clearly demonstrating that a considerable reduction in the average gradients in the plasma outer region can be obtained not only with elongated shapes but also with shapes with negative triangularity at modest elongation. High positive triangularity can even lead to an SEF bellow unity.

Global confinement. If thermal conduction processes dominate the electron energy losses, the SEF directly multiplies the global energy confinement time. The SEF varies in space, being closer to one in the plasma center where the flux surfaces are less shaped and increasing towards the LCFS. If its value in the temperature gradient region is used, the corrected electron energy confinement time τ_{Ee}/s still exhibits a dependence on the shape (fig. 4). Applying the value of the SEF at the edge cancels almost all the variation of τ_{Ee}. It is then clear that confinement can be considerably enhanced by geometrical effects alone. But these are averaged in an unfoldable manner in the global confinement time and any intrinsic influence of the shape on transport properties will only be revealed by a local power balance analysis.

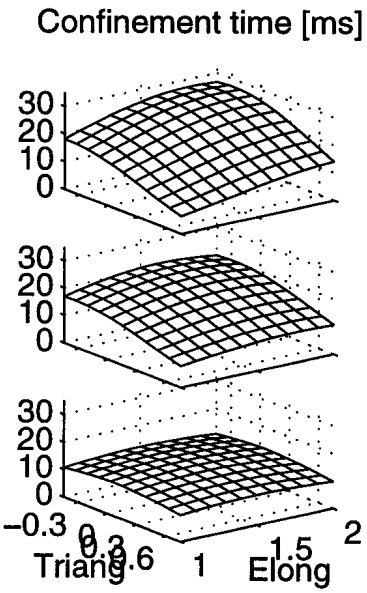

Fig. 4. At fixed value of $q_a = 4$ *and* $n_e = 5.5 \times 10^{19}$ m^{-3}, *dependence on the shape of (from top to bottom) : raw electron energy confinement time; corrected with SEF in the gradient region; corrected with SEF on the LCFS.*

Local transport. A simplified radial power balance was used in which: (i) the local ohmic power deposition is estimated from the current distribution obtained from an equilibrium reconstruction and a uniform electrical field; (ii) the radiated power is localised near the plasma edge [2] and has not been introduced; (iii) in the absence of an adequate measurement of the ion temperature T_i and its profile, ion and electron channel losses were not separated. Combining the power balance of both species leads to the definition of an effective thermal diffusivity χ_{eff} such that $q_{oh} = -n_e\chi_{eff}\,(dT_e/dr^*)\ s^{-1}$ and $\chi_{eff} = \chi_e + \chi_i\,(\nabla T_i/\nabla T_e)$, where q_{oh} is the input power flux. Well pronounced geometrical effects near the plasma edge are evident in the electron temperature profile (fig. 5): the mapped gradient at the edge is steeper for large SEF, indicating the beneficial effect of good flux surface separation and allowing a broader profile to build up. This generalises to all shapes as seen in figure 6 where the usual plot of the power flux

versus the temperature gradient is drawn. Given the rough assumptions made and the poor accuracy of a local power balance, no significative influence of the shape on the effective thermal diffusivity can be detected. The same observation is true for the gradient region, near r*/a = 3/4. Thus no dramatic changes in the transport coefficient are brought about by shape variation.

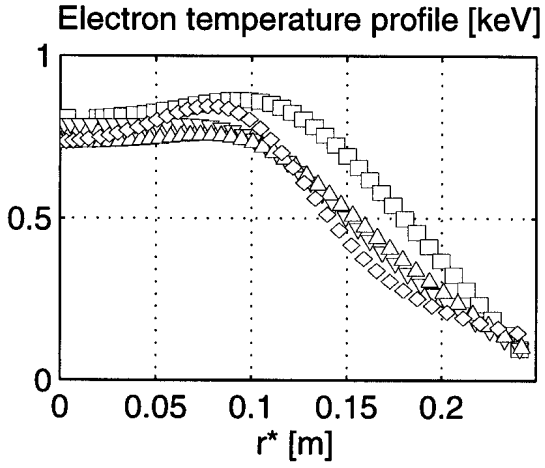

Fig. 5. Electron temperature profile mapped on the outer equatorial plane at $\kappa = 1.4$, $q_a = 2.5$ *and* $n_e = 5.5 \times 10^{19}$ m^{-3}:
□ δ = -0.3 SEF = 1.61
▽ δ = 0 SEF = 1.45
△ δ = 0.3 SEF = 1.29
◇ δ = 0.5 SEF = 1.00

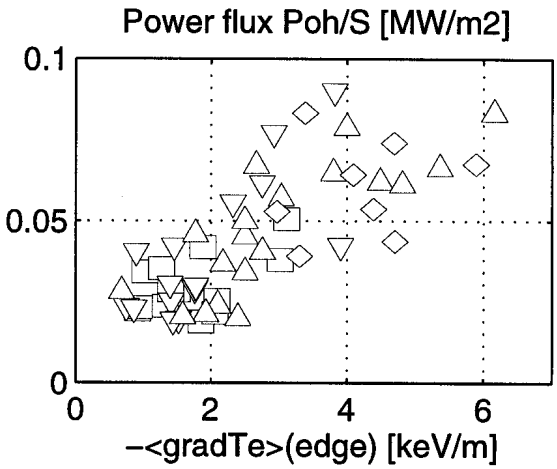

Fig. 6. Power flux near the edge versus electron temperature gradient for all shapes and currents at $n_e = 4.0 \rightarrow 5.5 \times 10^{19}$ m^{-3}. *For symbols see fig. 1.*

Conclusion. In summary, the large variation in global confinement time within the domain of explored shapes can possibly be explained by direct geometrical effects. No important influence of the shape on local transport coefficients has been found. Of course this statement may have to be revised in other operational regimes, for example with significant auxiliary heating or when approaching stability limits, as suggested by DIII-D [3]. This work however indicates that a global confinement optimisation can be achieved by tuning the plasma shape. Negative triangularity, which may exhibit poor MHD or vertical stability performance [4], is not the only option. More subtle shape variations can be envisaged and the result of this optimisation would be a compromise between the benefit of the geometry and other constraints.

This work was partly supported by the Fonds National Suisse de la Recherche Scientifique.

[1] F. Hofmann, M.J. Dutch, J.-M. Moret, *22nd EPS Conf. on Cont. Fusion and Plasma Phys., Bournemouth, 1995,* p. 101, vol. 19B part II.

[2] H. Weisen et al., *Measurement and Modelling of Light Impurity Behaviour in TCV*, this conference.

[3] A.W. Hyatt, E.A. Lazarus, T.H. Osborne, *21st EPS Conf. on Cont. Fusion and Plasma Phys., Montpellier, 1994,* p. 14, vol. 18B part I.

[4] M.J. Dutch, F. Hofmann, O. Sauter, D.J. Ward, M. Anton, J.-M. Moret, *22nd EPS Conf. on Cont. Fusion and Plasma Phys., Bournemouth, 1995,* p. 77, vol. 19C part IV.

Breakdown in a Continuous Low Resistivity Vessel in TCV

J.-M. Moret, F. Hofmann, B.P. Duval, J.B. Lister

Centre de Recherches en Physique des Plasmas
Association EURATOM - Confédération Suisse
École Polytechnique Fédérale de Lausanne, CH-1015 Lausanne, Switzerland

The TCV vacuum vessel is continuously welded and has a low toroidal resistance (45 μΩ) for passive stabilisation the plasma vertical motion. Consequently large vessel currents, up to 200 kA, are induced by the loop voltage during breakdown. They create a vertical magnetic field of the order of 10 to 20 mT that must be carefully compensated to achieve discharge breakdown. This compensation as well as the creation of a poloidal field quadrupole rely on accurate magnetic measurements and a precise model of the electromagnetic properties of the vacuum vessel.

Magnetic diagnostics. TCV magnetic measurements consist of: (i) 38 poloidal flux loops wound on the outside of the vessel: (ii) 4 arrays of 38 magnetic probes measuring the tangential field inside the vacuum vessel; (iii) one flux loop on each of the 23 poloidal field coils; (iv) 20 current sensors for the poloidal and toroidal field coils. In addition to an accurate calibration, the consistency of all these measurements has been enhanced by small corrections in their calibration and in the sensor position, leading to an error better than 0.5 mWb and 0.5 mT for the flux and field values, and about 1 mm for their position [1].

Vessel model. The vacuum vessel is made of stainless steel, 15 mm thick in the cylindrical parts and 20 mm thick on the top and bottom. Port holes in the vessel make its electromagnetic modeling difficult. Instead of a complicated 3-D representation, a toroidaly symmetric model with an experimentally determined spatial distribution of the effective resistivity was chosen. The vessel is divided in current filaments I_v whose voltage equation writes

$$0 = R_{vv}\, I_v + M_{vv}\, dI_v/dt + M_{va}\, dI_a/dt \qquad (1)$$

R_{vv} is the diagonal matrix of the sought filament resistances, I_a are the currents in the active coils and the M's are the mutual inductance matrices. These depend only on the geometry and are assumed to be known exactly. Trapezoidal current waveforms much longer than the vessel time constant (13 ms) are separately injected in each active coil. During the ramps I_v and dI_a/dt are constant and from eq. (1) one derives the vessel currents

$$I_v = -\, Y_{vv}\, M_{va}\, dI_a/dt, \qquad (2)$$

where $Y_{vv} = R_{vv}^{-1}$. The flux and field measured by the magnetic sensors are

$$\begin{aligned} \psi_f &= M_{fa}\, I_a + M_{fv}\, I_v \\ B_m &= B_{ma}\, I_a + B_{mv}\, I_v \end{aligned} \qquad (3)$$

The vessel filament resistances can be deduced from these measurements by solving for Y_{vv} in a least square sense the equations

$$\begin{aligned} \psi_f - M_{fa} I_a &= M_{fv} I_v = - M_{fv} Y_{vv} M_{va} dI_a/dt \\ B_m - B_{ma} I_a &= B_{mv} I_v = - B_{mv} Y_{vv} M_{va} dI_a/dt \end{aligned} \qquad (4)$$

The differences in the rhs are calculated using the flux and field values during the current flat top. In fact the available data allow the determination of only a limited number of filament resistances. Thus the latter are combined either in vessel segments, appropriate base functions or vessel eigenmodes by mean of a rectangular matrix T_{vw} and by replacing Y_{vv} by $T_{vw} Y_{ww}$ in eq. (4). Figure 1 compares the measured vessel resistivity with a rough estimation obtained from the vessel geometry and its specific resistivity. The influence of the ports holes is clear and leads to an average discrepancy of 20% which must be accounted for in programming the breakdown field.

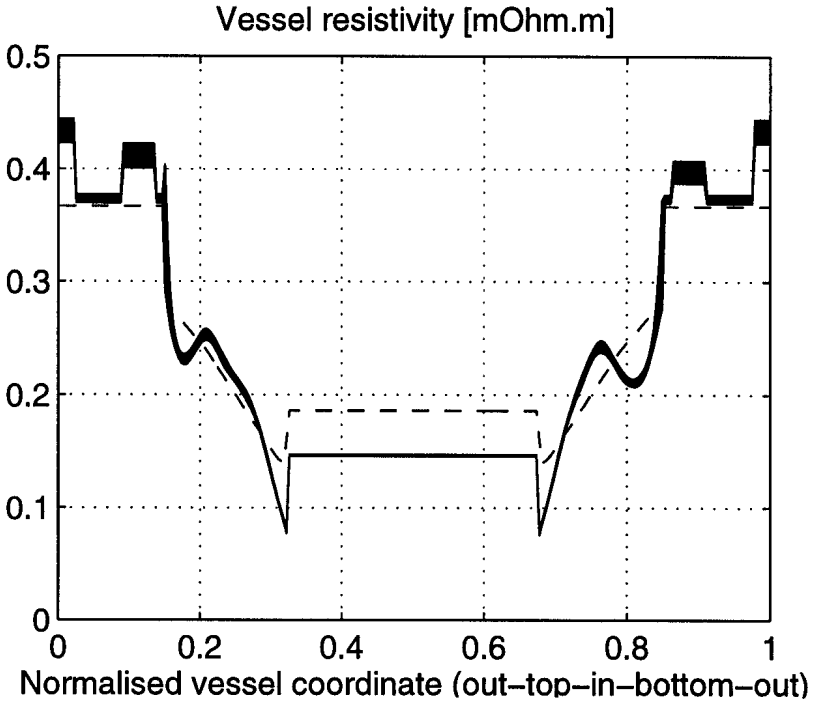

Fig. 1. Vessel resistivity distribution along the vessel perimeter. Dotted line: constructional estimate. Solid: measurement and its error.

Estimatin of the magnetic field configuration. The basic ingredients in determining the magnetic field topology inside the vacuum vessel prior to plasma breakdown are the currents in the active coils and in the vessel. These can be derived from the magnetic measurements by solving in a least square sense and with appropriate weights the set of equations

$$\begin{aligned} \psi_f &= M_{fa} I_a + M_{fv} I_v \\ B_m &= B_{ma} I_a + B_{mv} I_v \\ J_a &= I_a \end{aligned} \qquad (5)$$

The last equation has been introduced to account for errors between the measured (J_a) and adjusted (I_a) coil currents. This method however has proven inadequate and gave a poloidal field null location that did not coincide with that of the breakdown seen on H_α detectors. Equation (1) was then also used to account for the time dependent vessel currents in a consistent way. This new set of equations (5+1) is then solved over a time period prior to breakdown, using a two point difference operator for the time derivatives. The difference in the vessel current distribution estimated by these two methods is large (fig. 2). The latter however results in a estimation of the field inside the vessel and has been extensively used to optimise

the breakdown conditions. The drawback is the large size of the system to be solved, typically 6000 x 2000. To circumvent this, a Kalman filter was set up [2] which works as a best state estimator for the state space system whose states are (I_a,I_v), whose inputs are dI_a/dt and whose outputs are the (ψ_f,B_m,J_a). This approach gives comparable results at much reduced computation time. Because it is fast and it relies only on past samples, it could be implemented in real time as part of the future TCV digital control system.

Creation of plasma breakdown. Breakdown conditions are established in TCV by the MGAMS plasma control algorithm [3]. As part of the shot preparation, MGAMS computes the coil currents as functions of time such that the poloidal field vanishes at the desired breakdown position, at time t=0. In addition, we prescribe a positive vertical field gradient, dBz/dr > 0, in order to ensure vertical stability of the initial plasma. These calculations involve a complete simulation of the experiment, including induced currents in the vacuum vessel and plasma current startup. The main difficulty with this approach is that the precision of the poloidal field configuration that can be achieved in the experiment depends on the accuracy of the tokamak model used in the simulation. In TCV, this problem is particularly severe since the vacuum vessel has very low toroidal resistance. Reliable breakdown at loop voltages of the order of 10V can only be achieved when the poloidal field errors are less than about 0.5mT. This accuracy can be obtained by adding small corrections to the prescribed values of Bz, Br, dBz/dr, dBr/dr, at the desired breakdown position, at time t=0. The corrections are deduced from off-line vacuum field analysis, as described in the previous paragraph.. Plasma breakdown has been set up at various position in the vessel: z = 0, ±0.23 and ±0.40 m, for both directions of plasma current and of toroidal field. In all situations the vessel currents is similar to that plotted in figure 2. An example of the magnetic field configuration prior to breakdown is shown on figure 3 (left) for z = -0.23 m. The field modulus is less than 1 mT in a region of more than 0.2 m in diameter. The example on the right of this figure is the field configuration for a simultaneous breakdown at z = ±0.40 m used for the creation of a doublet [4].

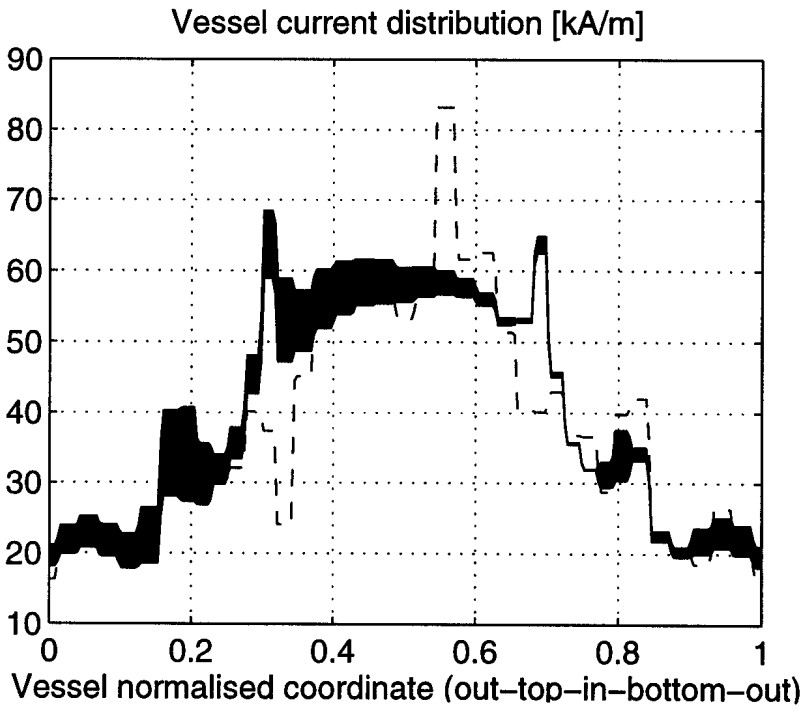

Fig. 2. Vessel current distribution along the vessel perimeter. Dotted line: estimation without vessel current dynamics. Solid: estimation with vessel current dynamics and typical error.

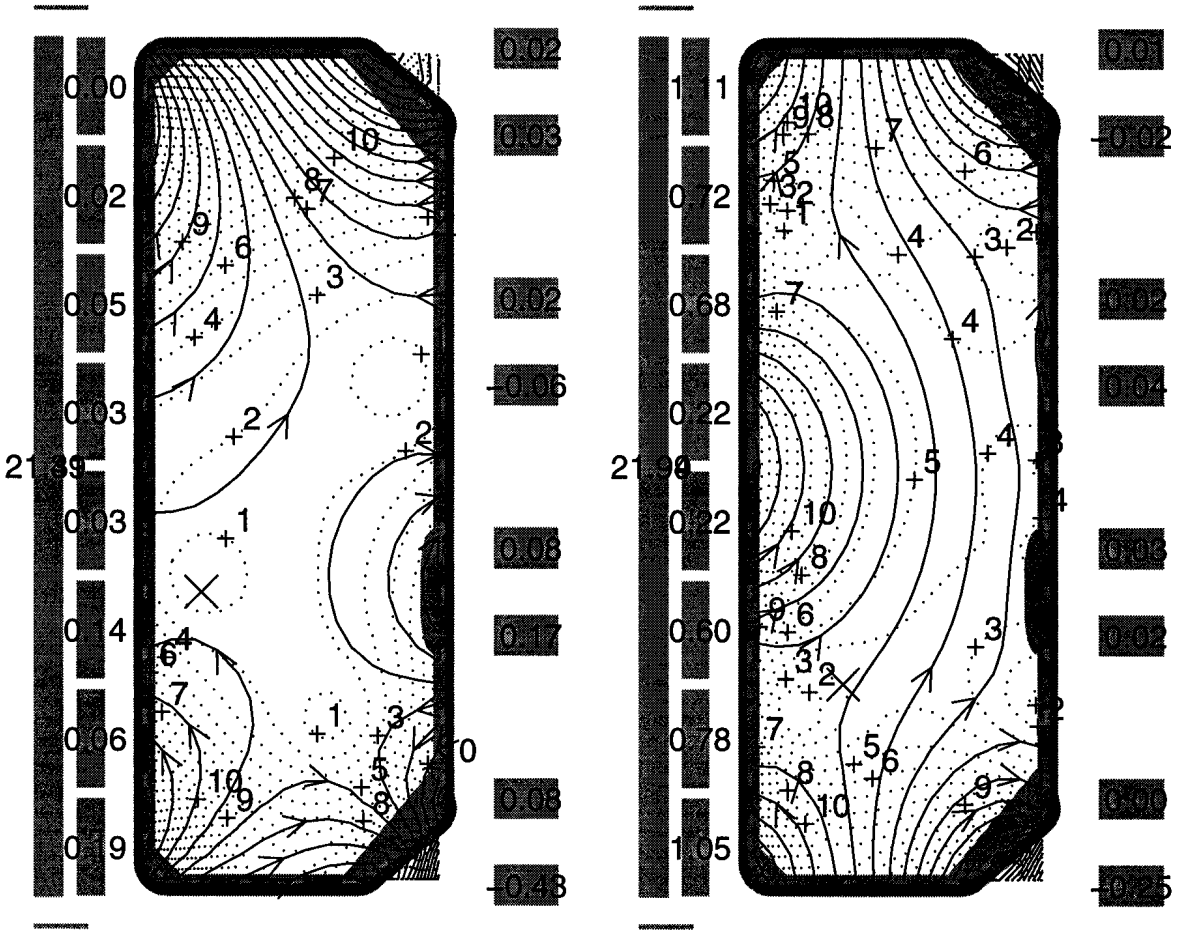

Fig. 3. Vacuum magnetic field configuration prior to plasma breakdown. Dotted lines are the magnetic field modulus contours labelled in [mT]. Numbers on the coils are their current estimation in [kA]. Left: breakdown at z = -0.23 m. Right: simultaneous breakdown at ± 40 cm for doublet creation.

This work was partly supported by the Fonds National Suisse de la Recherche Scientifique.

[1] J.-M. Moret, F. Buhlmann, F. Hofmann, G. Tonetti, *22nd EPS Conf. on Cont. Fusion and Plasma Phys., Bournemouth, 1995,* p. 417, vol. 19B part I.

[2] F.L. Lewis and V.L. Syrmos, *Optimal Control,* 2nd edition, John Wiley & Sons, New-York, 1995.

[3] F. Hofmann, M.J. Dutch, J.-M. Moret, *22nd EPS Conf. on Cont. Fusion and Plasma Phys., Bournemouth, 1995,* p. 101, vol. 19B part II.

[4] F. Hofmann, M.J. Dutch, J.B. Lister, Y. Martin, J.-M. Moret, *On the Possibility of Creating Doublet-Shaped Plasmas in TCV,* this conference.

Electron Density Profiles during Ohmic H-modes in TCV

Z. A. Pietrzyk, R. Behn, S. Franke, M. Anton, M.J. Dutch, B.P. Duval, F. Hofmann, Y. Martin, J-M. Moret, Ch. Nieswand and H. Weisen

Centre de Recherches en Physique des Plasmas, EPFL
Association EURATOM - Confédération Suisse
CH-1015 Lausanne, Switzerland

Ohmic H-modes have been obtained in the TCV tokamak ($R \approx 0.89$ m, $a \leq 0.25$ m, $B_T \leq 1.5$ T) in large range of configurations for different κ and δ [1]. For certain discharge parameters and wall conditions, long ELM free H-modes have been obtained. These ELM free H-modes terminate by a disruption or often by a transition to the L-mode during current ramp-down. Following the L-H transition, a rapid density increase is observed. In TCV this density increase can have either a flat or peaked profile. In such long lasting ELM free H-mode the particle transport can be studied to examine the difference between flat and peaked density profiles. The electron density profiles are measured using a 10 point repetitive (every 50 ms) Thomson scattering system together with a 6 channel interferometer. The behavior of the density in ELM free H-mode discharges for $\kappa \approx 1.66$ and $\delta \approx 0.43$ is described in this paper.

The initial high density increase, following the L-H transition, levels off to a plateau or low level density increase after 30 ms at the plasma edge and 200 ms at the center. Due to the rapid density increase at the plasma edge just after the L-H transition the electron density profiles are initially always flat or slightly hollow. The subsequent evolution can however lead to the formation of either a flat or peaked profile in an otherwise similar discharge as seen in Fig. 1 and Fig. 2 for Single Null configurations. Since the particle source is localized in the plasma periphery and the density profile is initially flat, the peaking in the case shown in Fig. 2 must correspond to a strong inward convection of particles.

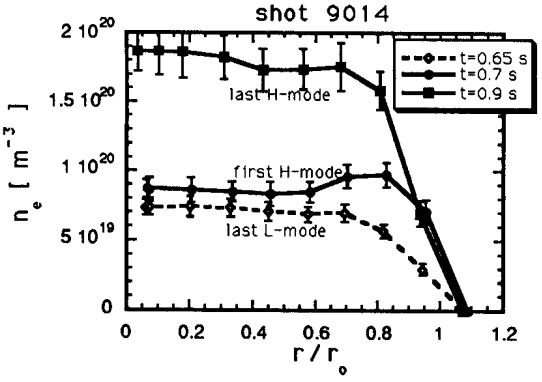

Fig. 1 Shot with flat electron density profile
$I_p = 426$ *kA*, $\kappa = 1.67$, $\delta = 0.42$

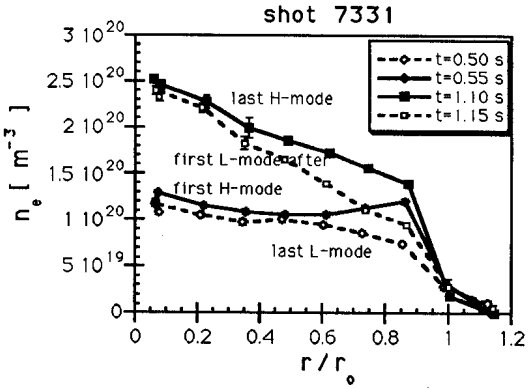

Fig. 2 Shot with highly peaked electron density profile
$I_p = 420$ *kA*, $\kappa = 1.64$, $\delta = 0.46$

L-mode -- dashed line, H-mode solid line in these figures.

We also observed cases where the density peaking occurs after a period where the profiles are flat or where the profile peaks only in the central part of plasma. The temperature profiles are very similar for both categories of density profiles. Since the electron temperature is always peaked and usually increases only near the plasma edge just after the L-H transition, the pressure profiles are peaked even for flat density profiles.

In order to determine whether the observed density peaking is due to impurity accumulation at the plasma center, we investigated the spatial and temporal variation of Z_{eff} obtained from multicore Bremstrahlung and reconstructed X-ray emissivity(2). In both cases (peaked and flat profile) the Z_{eff} profile remains flat or slightly hollow for the duration of the H-mode. This indicates that the observed spontaneous peaking of the density profile is not concomitant with central impurity accumulation. The overall impurity concentrations do however increase during ELM free H-modes, with Z_{eff} rising to near 3 after 0.5 seconds of ELM-free H-mode, but the rate of increase is the same for peaked and flat n_e profiles.

A study of the inversion radius q=1 and the sawtooth amplitude have been made using a soft X-ray tomographic reconstruction technique(3). The inversion radius and sawtooth relative amplitude (in "energy") is calculated from Single Value Decomposition (SVD) of the local emissivity matrix. The inversion radius increases rapidly at the L-H transition, which is expected from the rapid temperature rise (in about 10 ms) at the plasma edge, causing changes the current profile. However, shortly after transition, the inversion radius drops and is the same for both peaked and flat profiles. We observed a larger increase of the inversion radius for the flat than for the peaked profiles. The sawtooth amplitude decreases rapidly after the L-H transition and the decrease is the same for flat and peaked profiles. This behavior of sawtooth amplitude and inversion radius suggests that the flattening of the n_e profile is not simply a consequence of the reduced sawtooth activity.

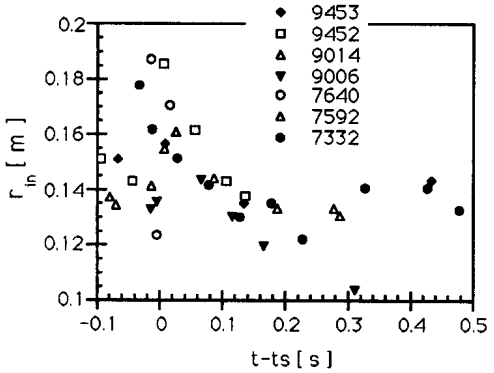

Fig. 3 Inversion radius (vertical) after transition solid points are the shots with peaked and open symbols refers to flat profiles for both of these figures

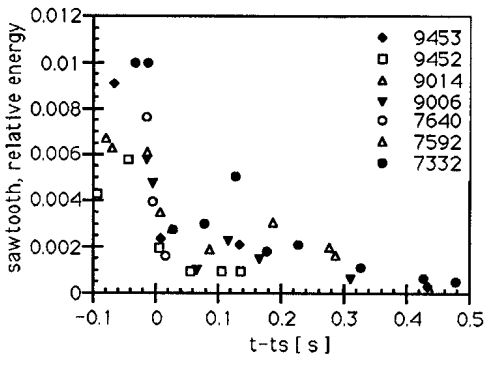

Fig. 4. Sawtooth "energy" from SVD of soft X-ray matrix

We examine particle transport in these H mode plasmas by calculating the diffusion coefficient and inward drift from the experimental data. At the L-H transition, as observed in other experiments a strong particle and energy barrier is created near the plasma edge. Therefore we assume that D is very small near the plasma edge in the H-mode. Due to limits on spatial resolution of the Thomson scattering system (about 4 cm) the n_e gradient cannot be resolved in this region. The expected gradient length of density near the plasma edge is about 1 cm. We analyze the central plasma region r/r_o=0.05 to 0.7, only, as r=0 has to be also excluded due to 1/r term in the equation.

The density profiles can be analyzed using the particle conservation equation in quasi-cylindrical approximation:

$$\frac{\partial n_e}{\partial t} + \frac{1}{r}\left(\frac{\partial}{\partial r}(r\Gamma_e)\right) = S_e. \qquad (1)$$

where: S_e is the electron source, which in our case is non-zero only at the plasma edge, so $S_e(r,t)=0.$ is assumed for our calculations. Γ is the particle flux which can be expressed as $\Gamma_e = - D \frac{\partial n_e}{\partial r} + n_e V$, where V is the inward pinch velocity. Substituting Γ_e into (1) after integration one gets:

$$D \frac{\partial n_e}{\partial r} - n_e V = \frac{1}{r} \int_0^r r \frac{\partial n_e}{\partial t} \, dr \qquad (2)$$

so that if n_e is known as a function of both r and t, we have an equation with two unknowns D and V. In the following calculations we assume that D and V are time independent functions during the ELM free H-mode. With this assumption one can write the equation (2) for two different times and this way gets two equations with two unknown D(r) and V(r). However it is possible to do this only for the peaked profiles since for the flat profile the first term is zero.

For flat profiles $\frac{\partial n_e}{\partial r} = 0.$ and, $-n_e V = \frac{1}{r} \int_0^r r \frac{\partial n_e}{\partial t} \, dr$ from which V(r) can be calculated.

It should have been realized that this is only a maximum V for which the flat profile can persist. Smaller V could also lead to flat profile as the plasma would be filled with particles, if there is a very small diffusion near the plasma edge, typical for the H-mode and larger in the rest of the profile. This can happen as the accumulation of the particles near the plasma edge would produced the gradient in the opposite to "normal" direction, thus the plasma interior would be filled by diffusion. Taking this to the limit a flat profile can exist with V=0.

and D≠0. The diffusion coefficient D cannot thus be determined from the experimental data for the flat profiles.

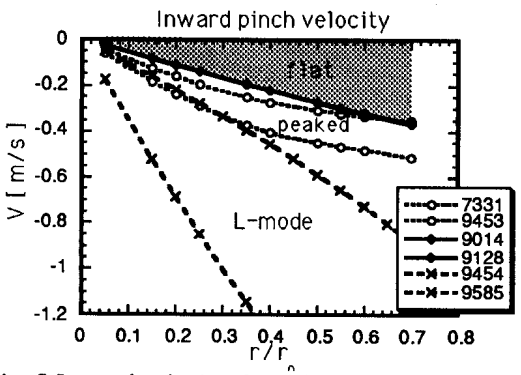

Fig. 5 Inward velocity for different plasma discharges,. solid line: max. V for flat profile, dotted lines: peaked H-mode profiles, and dashed: line L-mode.

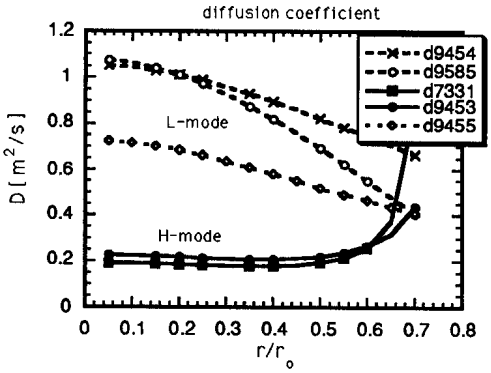

Fig. 6 Diffusion coefficient for selected L (dashed line) and H-mode (solid line) discharges (peaked profiles)

The radial dependence of the pinch velocity (Fig. 5) shows that the absolute value is always smaller in H-mode than in for L-mode and that flat profiles have a smaller inward velocity than the peaked profiles. Fig. 6 shows the difference between L-mode and H-mode diffusion coefficients. The L-mode diffusion coefficient, for shots with the same configuration as H mode but for which the H-mode was not achieved, is largest in the central part of plasma and larger than ELM free H-mode discharges. The diffusion coefficient for the H-mode increases with radial position. We know that at the edge it must become smaller, so a maximum must exist at some normalized radius between 0.6 and 1. Indeed, calculations performed for DIIID ELM free H-mode plasmas[4] gives the region of maximum D to be between r/r_O=0.3 and 0.7 and similar magnitude of D from 0.25 to 0.5 [m^2/s].

We have observed large differences of the density profiles for very similar global discharge parameters. Once the peaked profile is established it remain peaked till the end of ELM free H-mode period. A simple picture of particle transport shows that for the flat profile the inward drift is smaller than for the peaked profiles, which in turn is smaller than for L-mode discharges. Extending the range of plasma condition and shapes (q, κ, δ) in the future should give further insight into the physical processes leading to peaked density profiles.

Acknowledgments: This work was partially supported by the Fonds National Suisse de la Recherche Scientifique.

(1) Y. Martin at al at this Conference

(2) H.Weisen, D.Pasini, A.Weller and A.W. Edwards, Rev Sci. Inst. 62 (1991) 1531

(3) M. Anton at al at this Conference

(4) D.R. Baker and G.L. Jackson, APS 6Q23 Louisville, 1995

On the Possibility of Creating Doublet-Shaped Plasmas in TCV

F. Hofmann, M.J. Dutch, J.B. Lister, Y. Martin, J.-M. Moret
Centre de Recherches en Physique des Plasmas, EPFL
Association EURATOM - Confédération Suisse,
CH-1015 Lausanne, Switzerland

1. Introduction

Doublet-shaped plasmas were studied at General Atomics for many years [1,2]. Research in this field was stopped in 1984, when Doublet III was converted into DIII-D. Recently, the doublet has received renewed interest [3] because it has an intrinsic zone of negative shear, which is tied to the magnetic configuration and does not depend on a hollow current profile. Negative magnetic shear is thought to have beneficial effects on plasma confinement in tokamaks [4]. Another important property of doublets is the fact that vertical instability growth rates are much lower than in D-shaped plasmas with the same overall elongation [3].

In this paper, we consider three different scenarios for creating doublets and we summarize initial experimental work in this field on TCV.

2. Theoretical Scenarios for Creating Doublets

2.1. Lateral Constriction of a Highly Elongated, Racetrack-Shaped Plasma

Figure 1. shows a sequence of theoretical free-boundary tokamak equilibria illustrating this scenario. Stability analysis of these equilibria shows that the vertical growth rate first increases, as the elongation grows, then goes through a maximum, and finally decreases. The maximum growth rate is reached at the time when the internal separatrix begins to form. Its value depends on the assumed profile functions. For typical TCV profiles, the predicted maximum growth rate is beyond the ideal stability limit and for this reason, no experimental work has been devoted to this scenario so far.

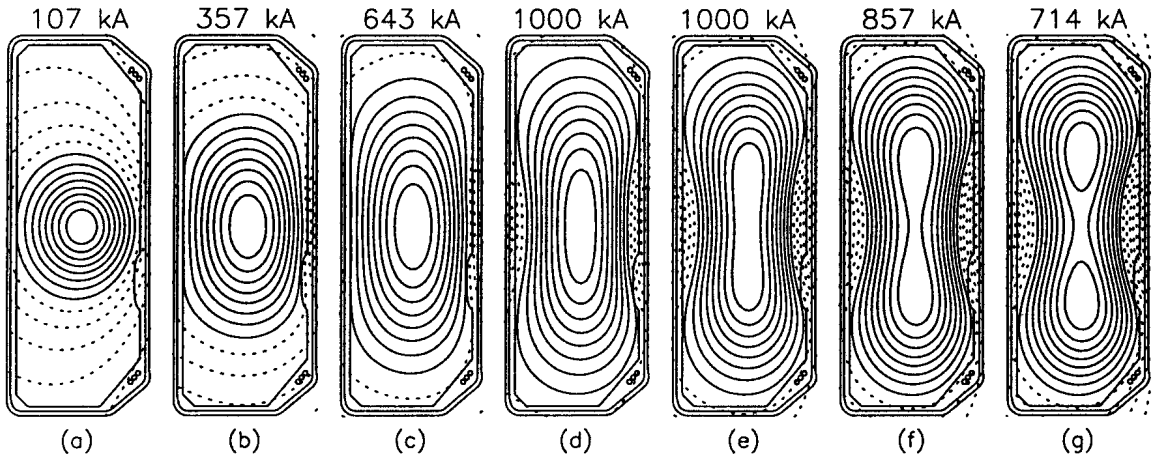

Fig.1. Theoretical scenario for creating doublets by lateral constriction

2.2. Hour-glass scenario

This scenario (Fig.2.) starts with a pear-shaped plasma representing the upper lobe of the doublet. The poloidal flux is controlled in such a way that it stays constant on the boundary of the final doublet shape. When the current is gradually increased under these conditions, the plasma spills over into the lower lobe, an internal separatrix appears and finally the currents in the two lobes become equal.

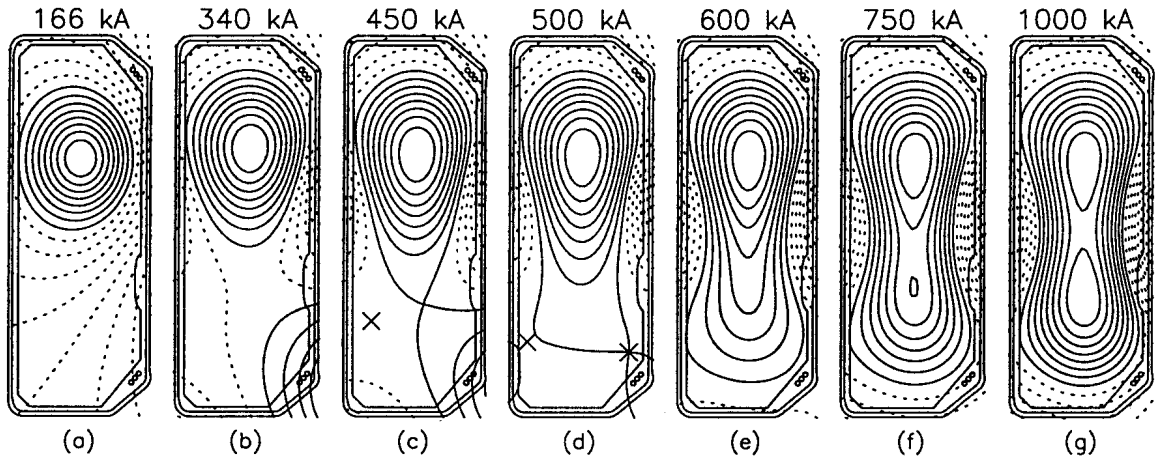

Fig.2. Theoretical scenario for creating doublets by "spill-over"

However, the existence of the intermediate equilibria in this scenario depends on the assumed current profile. For broad current profiles, all equilibria exist, as shown in Fig.2., whereas for peaked profiles, the highly asymmetric doublets (Fig.2e) can not exist in the sense that they cannot be generated with the TCV poloidal field coils. The boundary between existing and non-existing equilibria manifests itself by an extreme sensitivity of the plasma shape to small variations in the coil currents.

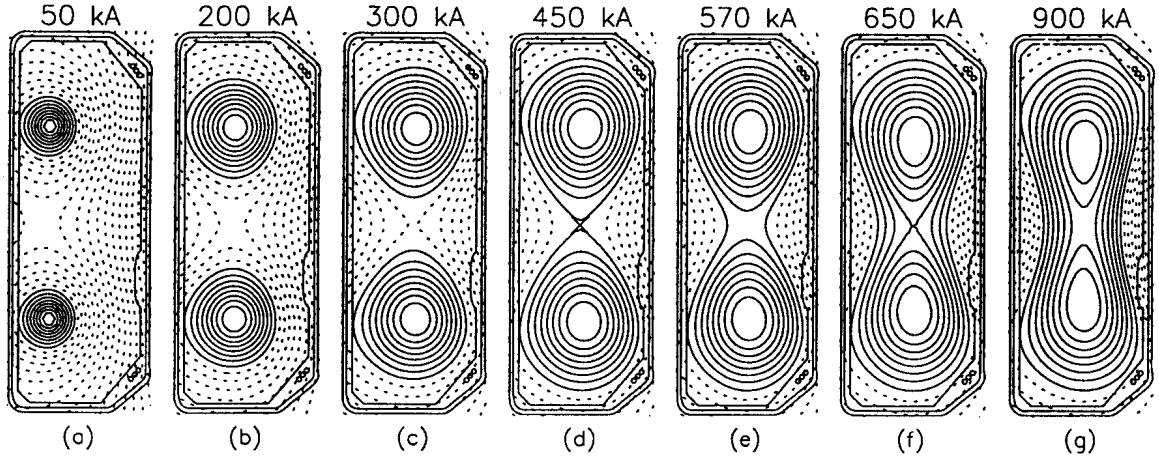

Fig.3. Theoretical scenario for creating doublets by merging two plasmas

2.3. Merging of two Droplet-Shaped Plasmas

This was the preferred scenario in the original doublet experiments at GA [2]. A sequence of theoretical equilibria based on TCV geometry is shown in Fig.3.

3. Doublet Experiments in TCV

3.1. Pear-Shaped Plasmas

The hour-glass scenario described above has been investigated experimentally in TCV: Pear-shaped plasmas have been created in the upper half of the vacuum vessel and a constant flux has been produced on a doublet-shaped contour (Fig.4.). However, when the current is increased, q drops below 2 before the plasma spills over to the lower lobe. This behaviour seems to be connected with the shape of the current profile. Plasma current profiles cannot yet be measured directly on TCV, but we can get some information on the width of the profile from equilibrium reconstructions. We find that in TCV ohmic plasmas, the profiles are rather peaked. If we try to compute the theoretical scenario (Fig.2.) using current profiles resembling the experimental ones, we discover that some of the intermediate equilibria cannot be generated and that the end of the experimental scenario (Fig.4.) roughly corresponds to the boundary between existing and non-existing equilibria.

The hour-glass scenario may be feasible in the future, when current profile modification with ECRH will become possible on TCV.

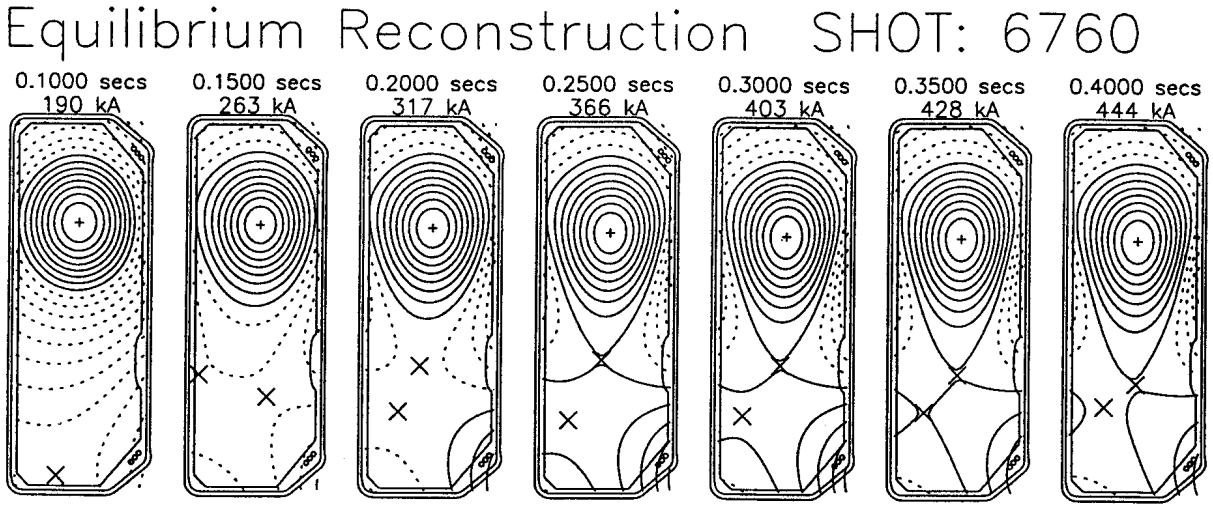

Fig.4. Experimental TCV equilibria showing the initial phase of the hour-glass scenario

3.2. Merging of two Plasmas

The TCV poloidal field coil set allows the creation of two quadrupole nulls inside the vacuum vessel, as described in [5]. In order to create two plasmas, the breakdown at the two nulls must be exactly simultaneous, because if one plasma starts up slightly too early it destroys the field null for the other plasma. If the two currents are roughly equal, they can both grow and finally merge to form a doublet. Initial experiments along these lines have produced doublet shaped plasmas with Ip=110kA and κ=2.6, lasting for about 10ms. As an example we show the reconstruction of an experimental equilibrium (Fig.5a). Plotting this result in κ-I_p space, together with the TCV data base, shows how far the doublet lies from all other plasmas produced in TCV up to now (Fig. 5b).

Acknowledgements: It is a pleasure to acknowledge the support of the entire TCV team. This work was partly supported by the Fonds National Suisse de la Recherche Scientifique.

References:

[1] T. Ohkawa et al., in Plasma Physics and Controlled Nuclear Fusion Research 1974 (Proc. 5th Int. Conf. Tokyo, 1974), Vol. 1, IAEA (1975) 281.

[2] J.C. Wesley et al., in Plasma Physics and Controlled Nuclear Fusion Research 1980 (Proc. 8th Int. Conf. Brussels, 1980), Vol 1, IAEA (1981) 35.

[3] L. Degtyarev et al. in Controlled Fusion and Plasma Physics (Proc. 21st Eur. Conf. Montpellier, 1994), Vol 18B, Part II, EPS (1994) 556.

[4] S.H. Batha et.al., in Controlled Fusion and Plasma Physics (Proc. 22nd Eur. Conf. Bournemouth, 1995), Vol 19C, Part II, EPS (1995) 113.

[5] J.M. Moret, et al., this Conference.

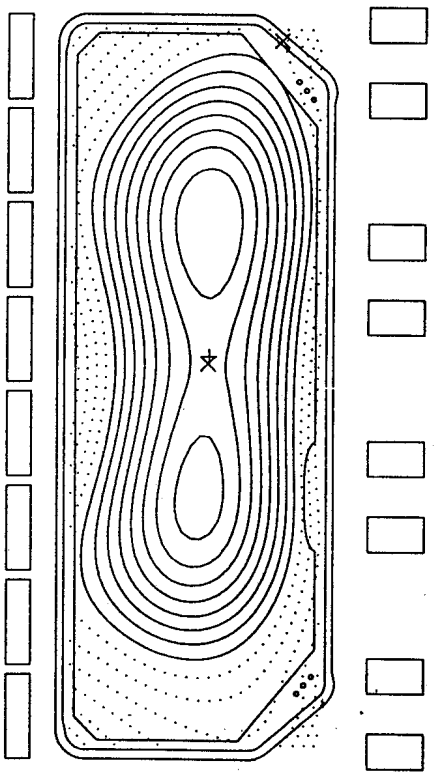

Fig. 5a. Reconstruction of experimental doublet equilibrium in TCV (I_p=110kA, κ=2.6)

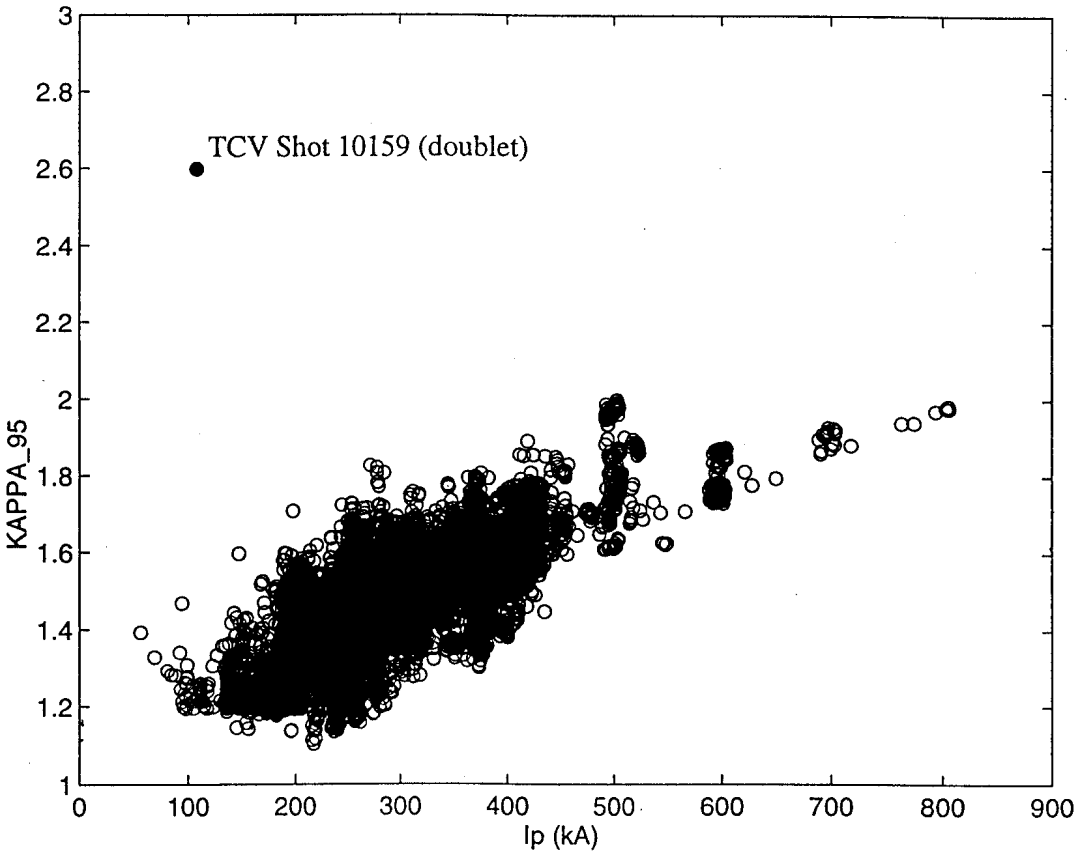

Fig. 5b. κ vs.I_p for TCV plasmas

Shape Dependence of Ohmic H-mode Accessibility in TCV

Y. Martin, B.P. Duval, J.-M. Moret, H. Weisen

Centre de Recherches en Physique des Plasmas,
Association Confédération Suisse-EURATOM,
Ecole Polytechnique Fédérale de Lausanne, 1015 Lausanne, Switzerland.

1. Introduction

TCV, (Tokamak à Configuration Variable), is a compact, highly elongated tokamak, built to study the influence of the plasma properties on the plasma shape. The design parameters are R=0.88 m, a≤0.25 m, Bt ≤ 1.5 T, $\kappa \leq 3$. 16 independent shaping coils allow precise control of shape parameters such as plasma elongation, triangularity, squareness, X-point(s) location and divertor geometry. Plasmas with up to 810 kA, $0.9 \leq \kappa_{95} \leq 2.1$ and $-0.45 \leq \delta_{95} \leq 0.7$ have to date been achieved. Since TCV does not, as yet, have auxiliary heating, power is provided to the plasma by the Ohmic heating only.

Following a first observation of a clear L-mode to H-mode transitions in a Single Null plasma discharge, H-mode transitions have been obtained in a large variety of limited and diverted, Single Null (SN) and Double Null (DN) configurations. All the L-H transitions, from ~600 discharges, have been compiled into a database containing plasma and configuration parameters during a short period preceding the L-H transition.

2. H-mode accessibility - operational domain

For the major configurations, L-mode to H-mode transitions have been obtained for plasma parameters in the ranges summarised in the table below. Ip and Bt are defined positive when anti-clockwise viewed from the top of the machine.

Configuration		Limited	SN	DN	
Mag. Field	(Bt)	1.0 & 1.4	-1.4, 1 & 1.4	1.4	[T]
Plasma Cur.	(Ip)	300 -> 600	-350 -> -280	230 -> 520	[kA]
	&		200 -> 450		[kA]
Plasma Dens.	(ne)	7.0 -> 11.0	2.5 -> 10.0	3.5 -> 11.0	[$10^{19}m^{-3}$]
Elongation	(κ_{95})	1.3 -> 2.0	1.05 -> 1.75	1.2 -> 1.7	
Triangularity	(δ_{95})	0.2 -> 0.45	-0.1 -> 0.65	0.35 -> 0.65	

Figures 1 and 2 plot all the documented L-H transitions for the major plasma parameters and the shape parameters respectively.The suffix '95' refers to the parameter value on the plasma surface enclosing 95% of the poloidal flux.

Such a presentation only attempts to show where H-mode plasmas have been observed. It does not imply that H-mode would not be achievable outside these domains. Thus, parameter values at the boundaries can not be considered as threshold values. As an example of this, the apparent limit at q=2 (fig 1) is due to MHD stability. The differences in plasma elongation and triangularity between the plasma configurations is due to the presence of a belt limiter in the vacuum vessel, which does not permit up-down symmetric plasma shapes. Moreover, the wide dispersion in the data, caused by diversity of the preprogrammed plasma conditions, indicates that the triggering of the L-H transition is probably not a simple function of any of these parameters.

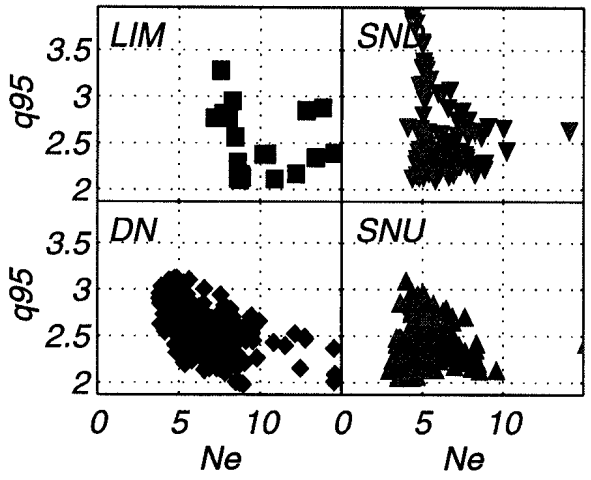

Fig1: H-mode accessibility in the ne q_{95} domain.

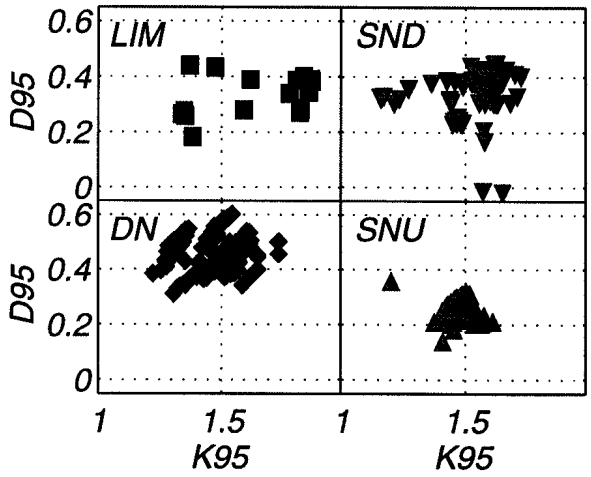

Fig 2: H-mode accessibility domain in the $\kappa\delta$ domain.

The global database approach does not thus allow the determination of the parameters responsible for triggering the L-H transition, so another approach is required. The versatile control system of TCV can be programmed such that the conditions of an L to H transition are reached by modifying each parameter separately. In order that the L-H transition occurs when required shape and plasma parameter values have been established, and not before, two startup scenarios have been developed. In the first , the distance between the inner wall and the plasma is increased from a limited configuration and is used in the next section.

In the second scenario, the plasma density is slowly increased after the desired configuration has been established. As already presented in [1,2], we found that the L-H transition occurred once the plasma density exceeded a certain value, called the "density threshold". This density threshold was shown to increase as the wall conditioning degraded and to increase with the plasma triangularity. The variations of the density threshold indicate that the density is not really a threshold in itself, but a parameter which acts on threshold parameters such as the edge temperature, density and/or their gradients. The fact that the first H-mode on TCV was obtained shortly after the first boronisation and that only after recent conditioning (by boronisation or He glow cleaning discharge), H-mode at densities lower than 3 10^{19} m^{-3} have been obtained, corroborate this impression. Moreover, when H-mode could not be obtained in conditions where it was expected, conditioning of the vacuum vessel often allows it to be recovered.

This influence of the wall conditioning on the H-mode implies that care must be taken to limit and quantify any changes in the vessel conditioning. This kind of experiment should be performed on a time scale of about an operating day, with as few intervening disruptions as possible, in order to avoid sharp degradations in the wall conditioning. The H-mode accessibility in the I_p-κ_{95} domain was examined on TCV following this prescription.

3. H-mode accessibility - I_p κ_{95} domain

To study the boundary of the H-mode operational domain, we performed a series of SND discharges with negative magnetic field such that the ion grad B drift is directed towards the X-point. A plasma with the desired elongation, triangularity and current was created in limited configuration, on the central column and the plasma density raised to a value above the expected H-mode threshold. The plasma was then moved off the wall resulting in a single null diverted configuration.

For each elongation in the range 1.05 →1.65, the plasma current was increased, from shot to shot, until an L-H transition occurred. Typically, when the plasma current was sufficient, the transition occurred when the inner gap was larger than ~1cm. The TCV shaping system allowed us to change κ_{95} with only minor changes in the other shaping parameters.

The lowest κ obtained (1.05) was limited by difficulties in creating these configurations with a set of discretely located shaping coils and the approach of the edge safety factor to $q_{95}=2$. The upper limit on κ (1.65) was in turn restricted by the vertical plasma stability. The installation of internal vertical control coils should allow this value to be increased.

Figures 3 show the results of the H-mode accessibility in the I_p - κ domain. Each discharge in the experimental series is represented by up to 3 symbols, linked by a line. Discharges in which an H-mode transition was not observed are indicated by hollow diamonds with time slices taken at 100ms intervals after the divertor was formed and the plasma density is being further increased. The H-mode accessibility boundary is revealed by the first discharges which show an H-mode transition. These discharges are represented in figure 3 by groups of symbols containing diamonds and a square. The time slices are indicated by: a) diamonds during the inner wall separation and b) a square just prior to the H-mode transition. The squares thus delimit the H-mode accessibility in that another discharge with higher I_p would also transit into H-mode. This boundary divides the I_p - κ graph into L-mode and H-mode regions, showing that more current is required for discharges with higher κ.

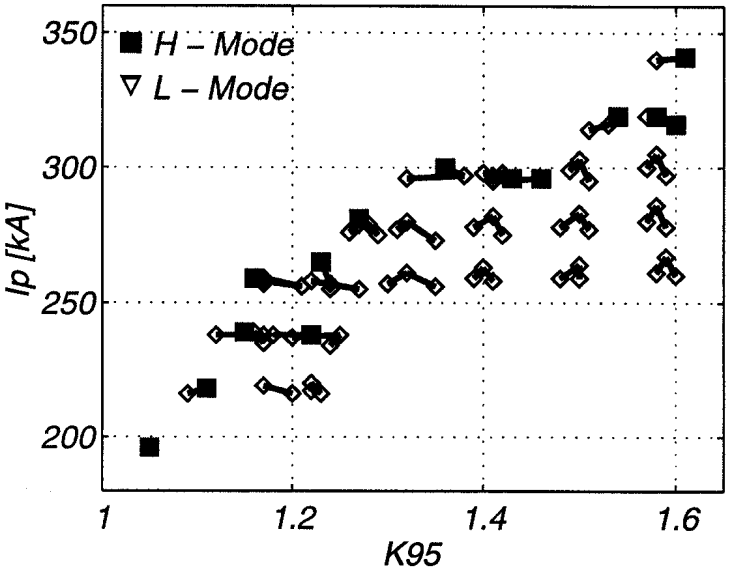

Fig 3: Squares represent the boundary between L and H-mode accessibility in the Ip -κ domain.

It is worth remarking that an Ohmic H-mode has been obtained with I_p lower than 200 kA and an almost circular discharge (κ ~ 1.05).

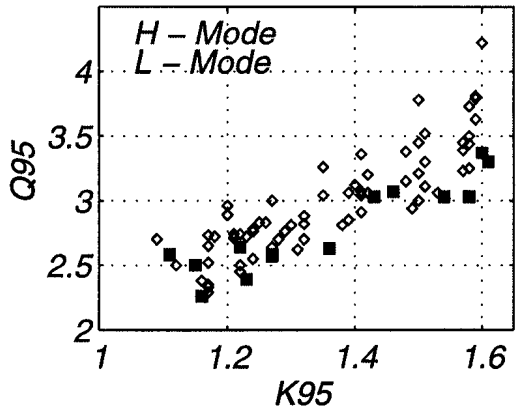

Fig 4: H-mode boundary limit in the q_{95} / K_{95} domain

The threshold values of the safety factor increase with the elongation, as shown in figure 4. This shows that the safety factor near the edge can not be a parameter which directly determines the threshold. Since the average plasma current density also varies at the boundary it can be similarly excluded.

Although this experiment did not allow us to determine the parameter responsible of the L-H transition triggering, a clear boundary was found in the Ip κ domain.

4. Discussion

The success of this experiment emphasises the importance of the configuration evolution in the determination of the boundaries of the H-mode accessibility domain. This must kept in mind when looking for threshold values of heating power. With additional heating, the input power may be approximately considered as a free parameter so the determination of a power threshold is possible. For ohmic heating, due to its dependence on plasma density, current and shape, a precise determination of the ohmic power threshold is difficult. However, from the database, the ohmic power which was applied to the plasma for all the compiled transitions can be plotted. The comparison of the ohmic power per unit surface against the product of the plasma density and the magnetic field, as shown in figure 5, with the ASDEX scaling represented by the solid line, indicates that the ohmic power is in the range of the usual power needed to get an H-mode. (The effects of radiation are neglected)

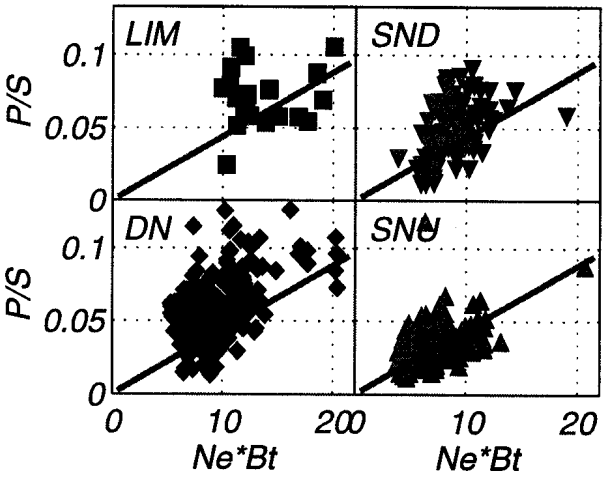

Fig 5: Ohmic power at the L-H transition compared with the ASDEX scaling.

5. Conclusion

Following boronisation, TCV has shown a remarkable facility to access H-mode with Ohmic heating alone. H-modes have been observed in virtually all categories of configurations (SND DND and limiter) and over a wide range of plasma parameters. The accessibility has been found to depend on the wall conditioning and, if this is sufficient, a minimum density and plasma heating current for a given configuration have been found necessary to obtain an H-mode transition. These threshold behaviours, indicate that other parameter(s) (such as edge density, temperature, or their gradients) may determine the occurrence of the L-H transition.

These experiments emphasise the requirement that a single parameter at a time be varied at least until the dominant factors have been determined.

As an example, the results of the H-mode boundary limit in the Ip-κ domain have been described. It is seen that less plasma current was required at lower values of κ with an H-mode obtained for a near circular plasma with $I_p \sim 200$kA. This demonstrates the ability of TCV to examine the H-mode threshold as a function of a single shaping parameter while keeping other parameters as constant as possible.

Acknowledgements: This Work was partly supported by the Fonds National Suisse de la Recherche.

References

[1] H. Weisen et al, *H-mode Workshop, Princetn,* 1995.
[2] Duval et al., 22th EPS Conference, Bornemouth, 1995.
[3] Ryter et al., 20th EPS Conference, Lisbon, 1993, ECA Vol 17C, I-23.

X-Ray Tomography on TCV

M. Anton, H. Weisen, M. J. Dutch, W. Von der Linden, I. Furno,

F. Bühlmann, R. Chavan, B. Marletaz, P. Marmillod, P. Paris

Centre de Recherches en Physique des Plasmas

Association EURATOM - Confédération Suisse

Ecole Polytechnique Fédérale de Lausanne, 1015 Lausanne, Switzerland

Abstract

The TCV tokamak ($B_T \leq 1.5$ T, R = 0.88 m, $a \leq 0.25$ m, $\kappa \leq 3$) is equipped with a soft X-ray tomography system consisting of 10 pin-hole cameras with 20-element planar Si diode arrays arranged around the plasma cross section. The aim of the diagnostic is to provide an independent measurement of the shape of the flux surfaces in the plasma core, to study MHD phenomena and to assist in the evaluation of the impurity content of the plasma. Successful commissioning of the system was dependent on the accurate determination of the actual camera geometries, the dimensions of which deviate within tolerances of ~0.1mm from their nominal values. It was also necessary to take account of the effect of the inactive 'dead' layer at the PIN diode surface causing angle- and spectrally dependent additional absorption, as discussed previously [1]. Several different pixel methods, including a novel method based on Fisher information, have been tested, both on simulated and on experimental data. The method based on Fisher information provides the most accurate reconstructions of both the overall emissivity profile and of small perturbations due to MHD modes. It has been used in investigations of the effect of plasma shape on sawtooth behaviour, showing a dramatic reduction at negative triangularity, of sawtooth amplitude, determined by application of the method of Biorthogonal Decomposition on the inverted data. The sawtooth inversion radius, determined using the same method, exhibits no significant dependence on triangularity [2].

Experimental determination of system geometry

Even small mechanical errors (0.1-0.2mm) can lead to substantial error in the reconstructions due to the small detector to aperture distances (~14 mm) and element separations (1 mm). Since it was impossible to achieve finer tolerances in the camera setup, which also has too satisfy severe constraints of vacuum tightness and thermal insulation, the departures of the actual geometry from the nominal one had to be determined experimentally. This was achieved by comparing the detected signals and simulated signals for several plasmas created at different positions in the elongated TCV vacuum chamber. The position and shape of these was obtained using the inverse equilibrium code LIUQE which uses external magnetic measurements. Once adjusted, no further geometrical corrections were necessary and reliable reconstructions using the initially determined geometry have now been obtained for more than one operational year.

Comparison of Pixel Methods

The poloidal cross section of the TCV has been divided into n_{pix} square pixels (3.8×3.8 cm^2) with emissivity $\mathbf{g}_i$ the contribution of which to the detected signals ($\mathbf{f}_j$) is described by a a tranfer matrix **T**:

$$\mathbf{f}=\mathbf{T}\mathbf{g}$$

Since the problem is underdetermined and the transfer matrix can be badly conditioned, we find a unique and sensible solution looking for a minimum of

$$\phi = \frac{1}{2}\chi^2 + \alpha R$$

where R is a regularizing functional and a is a positive number which determines the weighting between the goodness-of-fit, represented by χ^2, and the requirements imposed on the solution by R. The performance of different methods have been tested: First and Second Order Linear Regularization [3], Maximum Entropy [4] and a new method [5] relying on the Fisher Information (fig.1). In the case of the Minimum Fisher Information $R = |\nabla^2 g/g|$, as compared to First Order Regularization for which $R = |\nabla g|^2$. Computationally the Minimum Fisher Information reconstruction has been implemented as an iterative weighted first order regularization method, abbreviated MFR [2]. Independently of the noise affecting the data, the most faithful reconstruction are obtained with MFR (fig.1). Both linear regularization methods yield emissivity distributions which are too broad and Bayesian Maximum Entropy is too noisy. The good performance of the MFR is due to the fact that the smoothing is less strong where the Soft X-Ray emissivity is highest, i.e. at the plasma center.

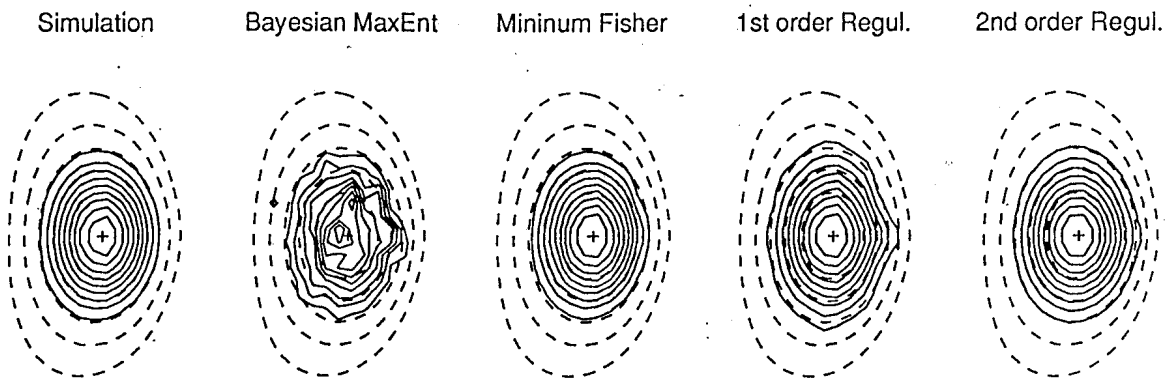

FIG. 1. Reconstruction of the simulated emissivity using different methods of inversion.

Dependence of sawtooth amplitude on plasma triangularity

For the analysis of sawteeth and MHD activity, we use the Biorthogonal Decomposition or SVD, applied to a time series of tomographic reconstructions. Let **X** be a matrix whose lines contain the time series of the different pixel emissivities, then the results of SVD is:

$$\mathbf{X} = \mathbf{U}^*\mathbf{S}^*\mathbf{V}^T$$

where the columns of the matrix **U** represent the spatial "eigenmodes", called *topos* , while the corresponding temporal information is contained in the columns of **V** or *chronos* [6].The pairs of *topos* and *chronos* are coupled by the elements of the diagonal matrix **S**, their corresponding singular values. The elements of **S** are stored in descending order, so that the first *topos /chronos* pair contains the most important features (fig. 2, top right). The contributions of different features is the relative signal energy

$$p_k = S_k^2/E_x$$

where S_k is a singular value and E_X is the sum of the squares of the diagonal elements of **S**.

In the example of fig. 2, from a reconstruction with 10 kHz time resolution, the most important *topos* (top, from left to right) have the appearances of an average emissivity profile (*topos* #1), an inversion profile (*topos* #2), and a pair of perturbations (#3 and #4) the sum of which corresponds to a rotating m=1 mode. The corresponding *chronos* shows that the inversion

profile changes sign at the sawtooth crash, when also the short burst of m=1 activity occurs. M=1 modes modulated by sawteeth are frequently observed on TCV.

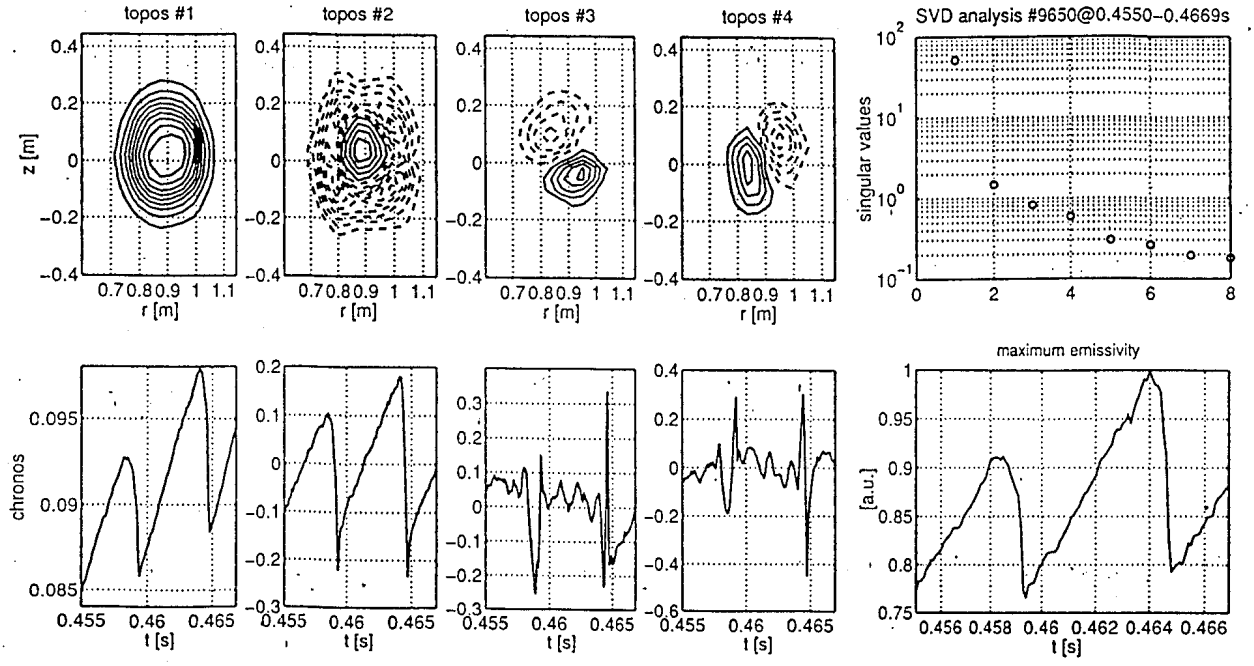

FIG. 2. SVD analysis of a reconstructed time series from TCV discharge #9650.

In TCV a strong correlation is observed between sawtooth amplitude and plasma triangularity. We investigated several time intervals during discharges where the triangularity was ramped down, using MFR and SVD as above. Fig. 3 shows that the relative sawtooth energies, determined from the corresponding singular values, decrease dramatically as plasma triangularity decreases. At negative triangularity the m=1 mode activity can become permanent, leading sometimes to mode locking and disruptions. Despite the reduction in sawtooth amplitude there is no significant dependence of sawtooth inversion radius on triangularity (fig.4). Discharges with negative triangularity have better confinement than discharges with positive triangularity [7]. The reduction in sawtooth amplitude with triangularity is consistent with the reduced ohmic heating power necessary to sustain discharges with negative triangularity.

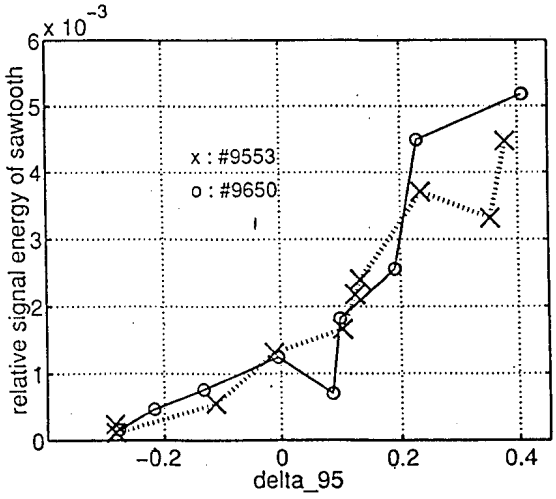

FIG. 3. Relative signal energy of the topos/ chronos pair representing sawtoothing as a function of the plasma triangularity.

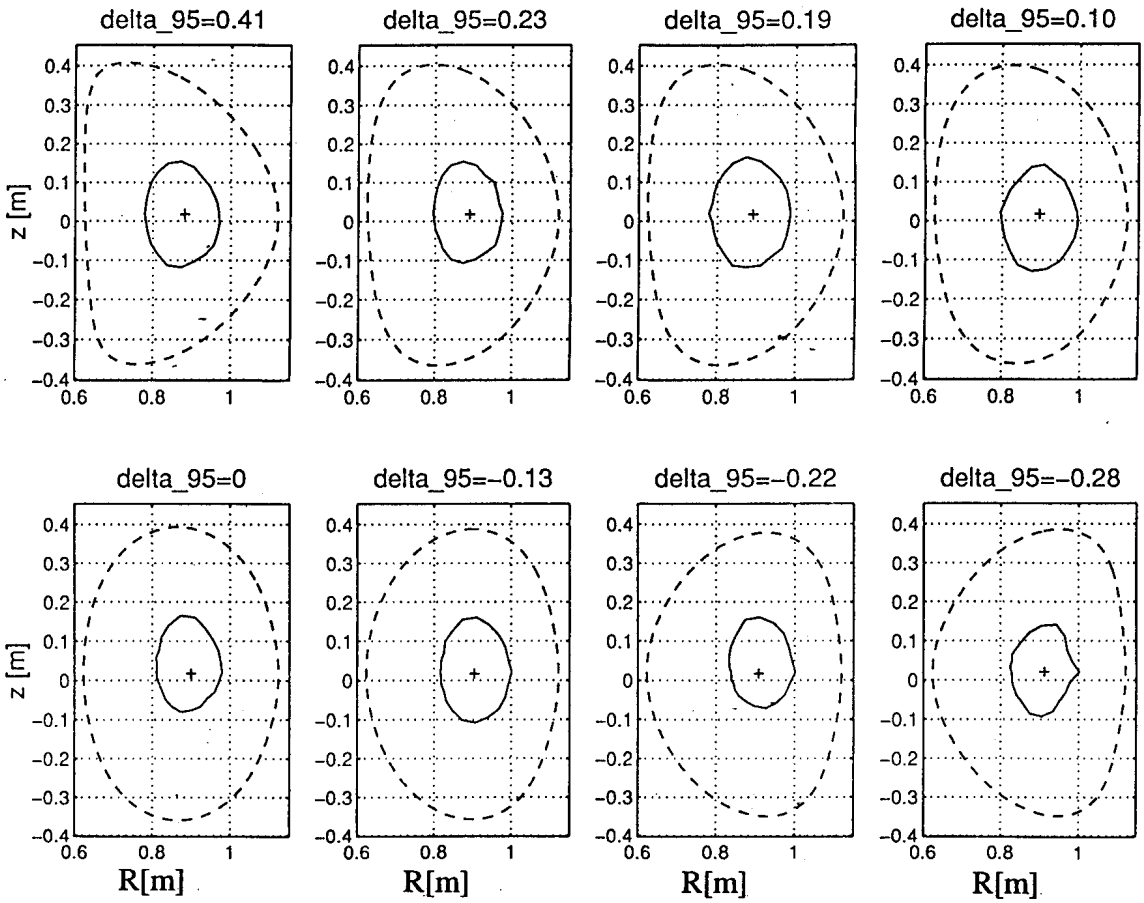

FIG. 4. Inversion radius deduced from the topos are shown with the last closed flux surface for different time intervals of TCV discharge #9650.

Acknowledgements

This work was partly funded by the *Fonds National Suisse de la Recherche Scientifique.*

References

[1] ANTON M, DUTCH M J and WEISEN, H: Rev. Sci. Instrum. **66** 7 p3762 (1995)

[2] ANTON M et al., X-Ray Tomography on TCV, submitted to PPCF

[3] PRESS, W H TEUKOLSKY, S A , VETTERING, W T, and FLANNERY, B P:

" Numerical Recipes in FORTRAN: The Art of Scientific Computing"

[4] VON der LINDEN, W:Appl. Phys. A **60** p155 (1994)

[5] FRIEDEN B R, Journal of Modern Optics Vol **35** 8 (1988)

[6] DUDOK DE WIT T, PECQUET A L, VALLET J C and LIMA R: Phys. Plasmas **1** (10)

[7] J M MORET, M ANTON, R BEHN et al, this conference

Measurement and Modelling of Light Impurity Behaviour in TCV

H. Weisen, V. Piffl+, A. Weller*, J. Moravec+, A. Krejci+, J. Raus+, M. Anton, R.A. Pitts, B. Joye, Ch. Deschenaux, R. Behn, F. Bühlmann, M.J. Dutch, B.P. Duval, S. Franke, F. Hofmann, Y. Martin, J.-M. Moret, Ch. Nieswand, A. Pietrzyk

Centre de Recherches en Physique des Plasmas
Association EURATOM - Confédération Suisse
Ecole Polytechnique Fédérale de Lausanne, Switzerland

+*Institute of Plasma Physics, Czech Academy of Sciences, Prague, Czech Republic*
**Max Planck Institut für Plasmaphysik, Garching, Germany*

Abstract. Light impurity radiation from the TCV tokamak is permanently monitored using a four-channel ultrasoft X-ray (USX) monochromator based on multilayer mirrors, allowing low-resolution ($\lambda/\Delta\lambda \approx 30$) measurements in the range 200-850 eV [1]. The strongest lines accessible to the instrument are responsible for about two third of the total radiated power of helium- and hydrogen-like ionization stages of the impurities Boron, Carbon, Nitrogen and Oxygen. The instrument can provide a direct measurement of radiation losses from H- and He-like light impurities. USX measurements and absolute emissivities from soft X-ray tomography [2] are used together with the IONEQ code to determine impurity levels. Total plasma radiation is obtained from three 16-channel bolometric cameras with nearly horizontal viewing lines.

Modelling of ionization equilibria using IONEQ

The ionization and radiation code IONEQ is used for modelling of emission from light impurities in TCV. The code uses measured electron density and temperature profiles from Thomson scattering and calculates radiation profiles associated with the main lines of each charge state of the impurity under consideration. It is however necessary to assume ad-hoc transport coefficients in order to obtain sensible results. In order to reproduce the observed line-brightness ratios of He- to H-like lines it is necessary to assume a diffusion coefficient $D \geq 0.5$ m^2/s [1]. By default we have adopted $D=1$ m^2/s. It is also assumed that the impurity concentration profile $c_z=n_z/n_e$ is constant in radius. This is equivalent to assuming the existence of an inward particle pinch with a profile which is adjusted as to produce an impurity density profile which match the measured electron density profiles. The comparison of predicted (for $n_z/n_e = 1\%$) and measured H-like line emission, which is only moderately sensitive to assumptions on transport coefficients, can be used for estimates of absolute impurity concentrations. IONEQ simulations with $0.5 \leq D \leq 2$ m^2/s show that the uncertainty on impurity concentrations based on USX line brightness measurements is a factor of 2. Additional uncertainties are associated with errors in the absolute instrumental throughput. Estimates of $Z_{eff} = 1 + \Sigma\, c_z(z-1)z$ with $(z=5,6,7,8)$ from USX and IONEQ alone are consistent with those from X-ray emissivity [3] and near infrared Bremstrahlung within the expected uncertainty.

The relative proportions of light impurities, such as $p_C=n_C/(n_B + n_C + n_N + n_O)$, are

used for quantitative interpretation of soft X-ray emission and are less sensitive to modelling assumptions than impurity concentrations. X-ray emissivities, normalized to $n_e n_i$, have been tabulated for the species of interest as a function of T_e using IONEQ [3]. Since most of the soft X-ray radiation, which is filtered using Be windows to contain only photon energies in excess of 1 keV, originates from fully ionized impurities in the core plasma, these emissivities are insensitive to assumptions on particle transport, and are hence more appropriate for absolute estimates of impurity concentrations. Soft X-ray based measurements of light impurity concentrations are however dependent on the assumption that the impurities monitored are responsible for most of the soft X-ray radiation. This assumption is supported by preliminary measurements of FeXVII line emission at 826 eV. The identification of the Fe line remained inconclusive because of the proximity of an OVIII line at 820 eV. The measurements however give an upper limit, $n_{Fe}/n_e \leq 10^{-5}$, at which level metallic impurities from untiled parts of the stainless steel vessel are expected to contribute less than 10% of the total soft X-ray emission.

The total power emitted from H and H-like light impurities, which contribute to radiation losses, can also be obtained from the measured line brightnesses. To this effect the radiation profiles calculated by IONEQ are volume integrated using the flux surface geometry from the equilibrium reconstruction. The estimate is fairly insensitive to assumptions on particle transport coefficients which only affect the position and width of the radiation shells. Note that although lower ionization stages may be responsible for a large fraction of the radiated power, their radiation is emitted too close to the plasma edge to make a significant impact on confinement.

Monitoring of impurity levels

Long term monitoring of vessel conditions is achieved by means of a reproducible 'standard discharge' in a Single Null diverted configuration, which is produced at least once every operational day. The relative proportions of light impurities undergo dramatic changes as a result of vessel conditioning such as glow discharge cleaning and boronization [4].

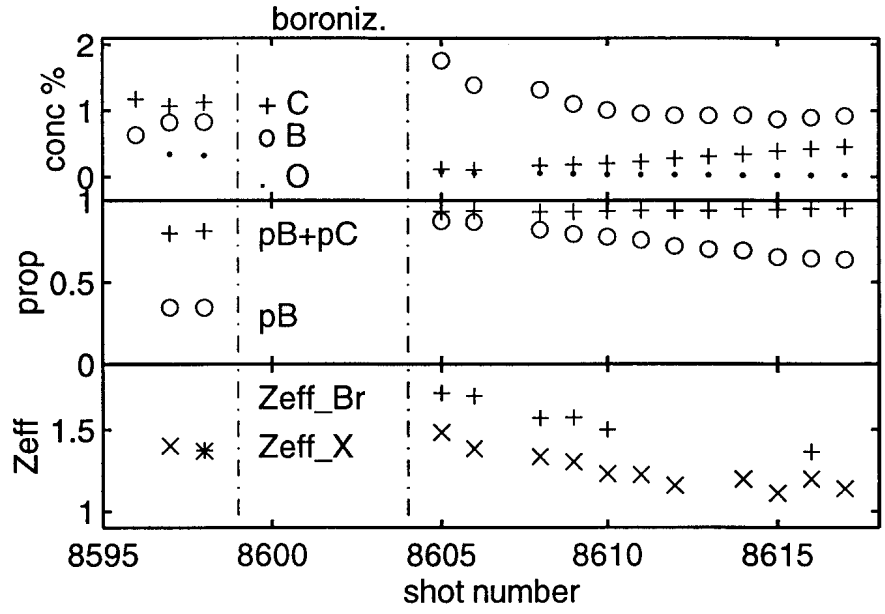

Fig.1 Evolution of light impurity concentration and plasma purity after a boronization

On the first discharge after a reboronization carbon levels are reduced by a factor of 10, Oxygen levels by a factor of 2-3, while Boron accounts for more than 90% of the light impurities (fig.1). Over the subsequent ~ 10-20 discharges Carbon and Boron concentrations return to their pre-boronization levels (~1%) while Oxygen levels continue to drop by a further factor of 2-3 to about 0.1%. After the first 10-20 discharges, impurity levels, including the reduced Oxygen level, remain fairly constant for hundreds of discharges.

Influence of discharge conditions and plasma shape

The core impurity concentrations were inferred from the tomographically reconstructed core X-ray emisivity together with light impurity proportions from USX measurements and IONEQ simulations for a wide range of inner-wall limited ohmic L-mode conditions ($120 \le I_p \le 600$kA, $3 \le \langle n_e \rangle \le 9 \times 10^{19} m^{-3}$, $1.1 \le \kappa_{95} \le 1.8$, $-0.3 \le \delta_{95} \le 0.5$, [5]). The corresponding values of Z_{eff} are shown versus $\langle n_e \rangle$ in fig.2 for $\delta_{95} \ge 0$, where the symbols refer to classes of ohmic power density at the last closed flux surface, P_{oh}/S. Low power and high density is favourable for plasma purity. These dependences were not observed for $\delta_{95} < 0$. In this set of experiments the proportion of Carbon increased with δ for $\kappa \ge 1.4$ (fig.3). The higher Carbon concentrations may be due to the higher ohmic power necessary to sustain discharges with high triangularity [5] and to differences in the boron coverage of the wall areas wetted by the SOL. During the course of these experiments (~150 shots) the part of Carbon in the impurity mixture of standard discharges increased from 0.4 to 0.6, suggesting a stronger than usual erosion of the Boron layer, possibly due to the higher power discharges in the series [4]. Despite the differences in the impurity mixture, the radiated power fraction P_{rad}/P_{oh}, as determined from bolometry, is remarkably independent of plasma shape, showing that differences in radiation losses cannot explain the reduction of energy confinement time with increasing triangularity [5].

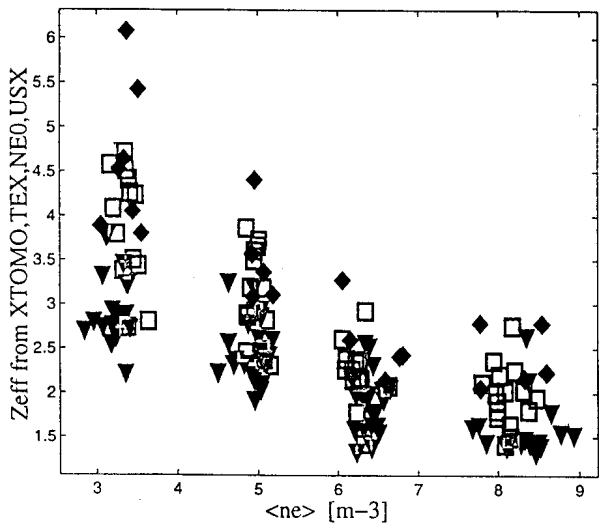

Fig.2. Dependence of core Zeff from X-ray tomography on line average density. Diamonds: 100 kW m^2>P_{oh}/S > 68 kW/m^2 Triangles: 42 kW/m^2>P_{oh}/S > 17kW/m^2

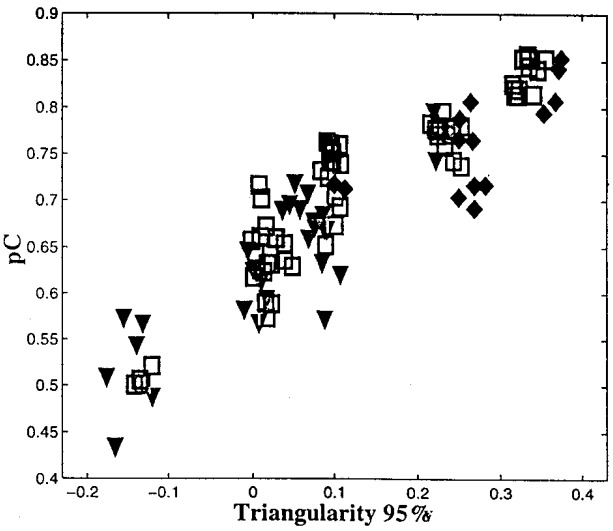

Fig.3. Dependence of Carbon proportion on plasma triangularity for κ>1.5. (For low δ no significant dependence) Squares : 68 kW m^2>P_{oh}/S > 42 kW/m^2

P_{rad}/P_{oh} depends mainly on the electron temperature near the LCFS (fig.4a), which itself increases with P_{oh}/Sn_e (fig.4b). In fig.4c the ratio P_{USX}/P_{rad} is shown to rise sharply as a function of Te(0.9a). The increase corresponds to changes in the dominantly radiating ionization stages, with He and H-like stages dominating at Te(0.9a) > 200 eV. Comparison of absolute values shows that the overall throughput of the USX diagnostic is underestimated by a factor of 2-3.

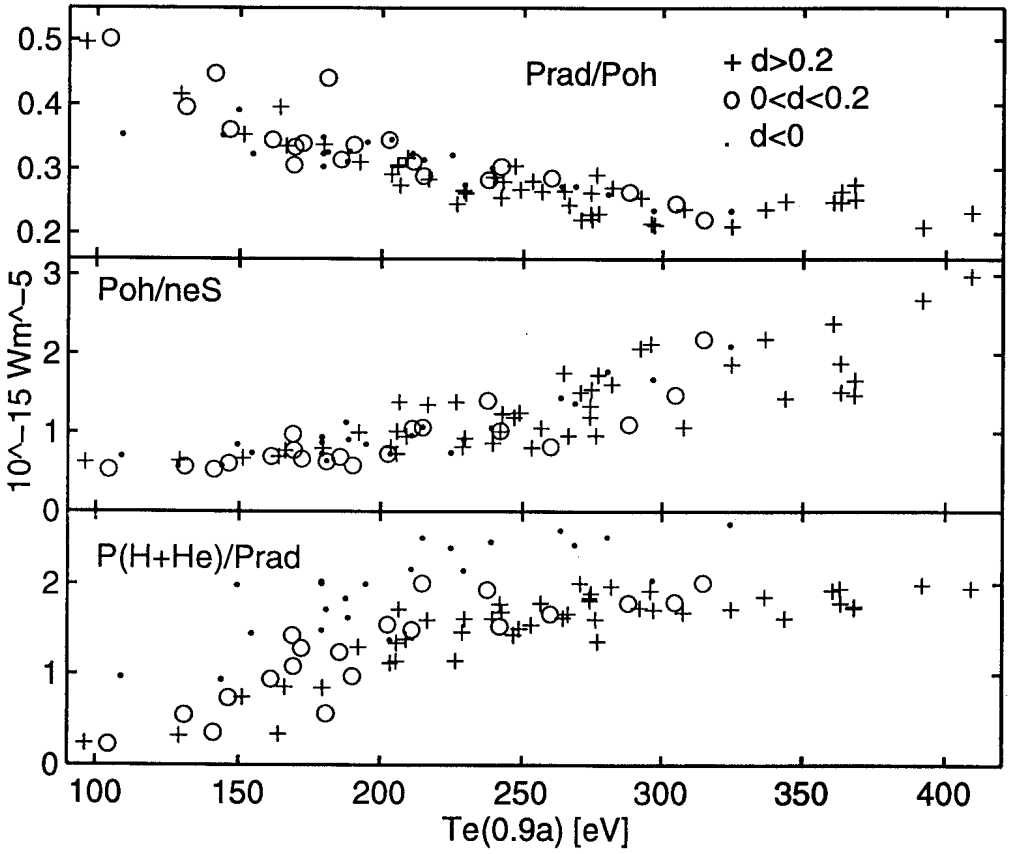

Fig. 4. Dependence of radiated power fraction (a) on edge temperature measured at r/a ≈ 0.9. Relation (b) between P_{oh}/Sn_e(0.9a) and Te(0.9a). Dependence (c) of ratio of H- and He-like radiation to P_{rad} on Te(0.9a). The set of data was restricted to intermediate values of elongation for clarity, 1.4<k<1.7. Symbols refer to classes of triangularity (+ δ>0.2, o 0<δ<0.2, · δ<0).

Conclusions. Altough the impurity mixture varies with plasma shape, overall impurity content and radiation losses depend mainly on edge conditions such as P_{oh}/S, Te(0.9a) and n_e. The dependence of energy confinement on triangularity reported in [5] cannot be accounted for by radiation losses. The USX 4-channel multi-layer mirror monochromator has proven to be a valuable diagnostic for monitoring the content and radiation losses of H- and He-like light impurities.

Ackn: This work was partly supported by the Fonds National Suisse de la Recherche Scientifique.

References:

[1] Weisen H, V. Piffl, A. Kreijci et al, 22nd EPS on CFPP, 1995, ECA 19C II-393
[2] M. Anton, H. Weisen, M.J. Dutch et al, this conference
[3] H. Weisen, D Pasini, A Weller & AW Edwards, Rev. Sci. Instrum 62 (1991), 1531.
[4] R. Pitts, Ch. Nieswand, H. Weisen et al, 12th PSI, St. Raphael, May 1996
[5] J.-M. Moret, M. Anton, R. Behn et al, this conference (oral presentation)